Mechanical Systems and Signal Processing 223 (2025) 111833

Contents lists available at ScienceDirect

Mechanical Systems and Signal Processing

journal homepage: www.elsevier.com/locate/ymssp

Wavelet-based generation of fully non-stationary random processes with application to seismic ground motions

Federica Genovese [a,b,*], Alessandro Palmeri [b,c,d]

[a] Department of Architecture and Territory, University "Mediterranea" of Reggio Calabria, Italy
[b] School of Architecture, Building and Civil Engineering, Loughborough University, United Kingdom
[c] Department of Structural, Geotechnical and Building Engineering, Politecnico di Torino, Italy
[d] Anchors Regulations and Code Development, HILTI Entwicklungsgesellschaft mbH, Germany

ARTICLE INFO

Keywords:
Circular wavelet
Signal processing
Earthquake engineering
Random processes
Artificial accelerograms
Structural dynamics

ABSTRACT

Assessing the performance of earthquake-resistant structural and geotechnical systems is crucial for achieving a desired reliability level and enhancing the resilience of the built environment in seismic-prone regions. Nonlinear dynamic analyses are widely used to quantify structural and geotechnical performance. Still, they require an accurate representation of nonlinear behaviours and proper modelling of the expected seismic events. Stochastic approaches are popular strategies for modelling dynamic actions to account for the uncertain nature of ground shaking. In this framework, joint time–frequency signal representations of seismic records are powerful tools to analyze signals' time-varying amplitude and frequency content. This paper presents a new method for the stochastic generation of artificial accelerograms using the circular harmonic wavelet transform, which possesses joint time–frequency localization capabilities and offers the engineers a clear and transparent interpretation of the results. The proposed approach adopts a new exponential auto-correlation structure for generating the random phases in the "child (generated) signals" starting from the deterministic ones in the "parent record". The effects of the correlation structure and different subdivisions of earthquake records in frequency bands are investigated and discussed, leading to practical considerations for identifying an effective trade-off between localization in time and frequency domains. The method can be used for seismic assessment and design purposes, and numerical applications illustrate its potency.

1. Introduction

Earthquakes pose one of the greatest threats to the built environment in terms of loss of human lives and widespread destruction. Triggered by immense forces acting deep within the Earth's crust, earthquakes result in complex three-dimensional movements of the Earth's surface, causing dynamic effects on structures and geotechnical systems that can severely compromise their functionality and stability. The ground shaking induced by an earthquake at a given location is random in nature and depends on several factors, such as the event's magnitude, the depth of the hypocentre, the distance to the epicentre, the density and mechanical properties of the Earth's strata through which the seismic waves have traveled, the local geological conditions immediately beneath the given site (e.g., local

* Corresponding author at: Department of Architecture and Territory, University "Mediterranea" of Reggio Calabria, Via dell'Università 25, 89124 Reggio Calabria, Italy.
E-mail addresses: federica.genovese@unirc.it (F. Genovese), dynamics.structures@gmail.com (A. Palmeri).

https://doi.org/10.1016/j.ymssp.2024.111833
Received 29 July 2023; Received in revised form 8 August 2024; Accepted 11 August 2024
Available online 4 September 2024
0888-3270/© 2024 The Author(s). Published by Elsevier Ltd. This is an open access article under the CC BY license (http://creativecommons.org/licenses/by/4.0/).

amplification in alluvial basins).

The accelerogram $\ddot{u}_g(t_\ell)$ is the time-discretized record of ground acceleration along a given direction, e.g., North-South, East-West, and up-down, where $u_g(t_\ell)$ is the ground displacement at time t, the over-dot is Newton's notation of time differentiation, and $t = t_\ell$ is the ℓth discrete time instant at which the ground acceleration is known. Accelerograms are recorded by accelerometers and, in case of strong ground motions, they are post-processed (e.g., baseline removal, reduction of low-frequency noise, etcetera [1]), classified, and made available through dedicated databases (e.g., PEER NGA-West2 database [2], PEER NGA-East database [3], Engineering Strong Motion (ESM) database [4], etcetera).

In the design practice, structural and geotechnical engineers use a range of tools to represent the expected seismic actions, including their aleatory variability. For conventional earthquake-resisting systems, intensity measures (IMs) such as *Arias intensity* [5], peak ground acceleration (PGA), and spectral pseudo-acceleration provide sufficient information to carry out seismic analyses and design checks. Advanced applications, however, require the numerical solution of the equations of motion for a suite of accelerograms, deemed representative of the seismic hazard at a particular site. When local, geologic, and tectonic conditions of a given location are similar to those of the sites where strong motions have previously been recorded, these time histories can be directly used as input. Otherwise, the use of artificial accelerograms, having characteristics consistent with those of actual earthquakes, could represent a valid alternative (e.g., [6–12]).

Stochastic simulation of artificial accelerograms is a valuable tool to account for ground motion randomness in reliability analyses (e.g., [13]), including the development of robust fragility curves that typically require a large number of earthquake records [14,15]. However, generating realistic artificial accelerograms can be challenging. For example, many signals that prima facie appear reasonable in the time domain may not be so in the frequency domain, and vice versa [16]. Furthermore, earthquake records are inherently non-stationary; hence, a joint analysis in time and frequency domains is necessary to overcome the limitations of the traditional Fourier analysis and accurately analyze the evolutionary spectral content of such signals [17–19].

Unlike the harmonic functions used in ordinary Fourier transform (FT), wavelets possess joint time–frequency localization capabilities (e.g., [20–22]), which enable their successful application in a range of structural dynamics problems. For example, Spanos and associates have employed various wavelet families, including *Newland's harmonic wavelets* [23,24], to compute the evolutionary power spectral density (EPSD) function of stochastic signals [25,26] and determine the response statistics of linear and nonlinear oscillators subjected to non-stationary excitations [27], all within the theoretical framework of Priestley's non-stationary random processes [28]. In [10], Wang et al. proposed a new generalized harmonic-wavelet (GHW) based formula to simulate non-stationary random processes by integrating the evolutionary spectral representation method. The formulation introduced in [10] is based on the relationship between the GHW coefficients of the random process and the EPSD of the non-stationary process. The samples of the random process are generated by superimposing the GHWs with the random phase angles uniformly distributed in the range from 0 to 2π. The use of GHW offers the advantages of orthogonality and complete coverage of the frequency domain without overlap. In addition, other researchers, such as Liang et al. [29], have demonstrated that the wavelet transform can accurately estimate the EPSD function from a single time-history record of the phenomenon under study. This body of research clearly shows the great potential of wavelet-based approaches when non-stationarity plays an important role in the dynamics of structural systems, such as in the case of seismic signals (e.g., [30–33]). In this context, explicit closed-form solutions have been derived by Basu and Gupta for the stochastic response of linear single-degree-of-freedom (SDoF) oscillators [34] and multi-degree-of-freedom (MDoF) structures [35] subjected to a non-stationary ground shaking whose time-dependent amplitude and frequency content are modeled through a generalization of the Littlewood-Paley (L-P) basis of orthogonal wavelets (e.g., [36]). Iyama and Kuwamura [37] have proposed a technique for simulating artificial accelerograms based on the inverse wavelet transform of a random sequence of wavelet coefficients satisfying some constraints in terms of instantaneous energy for each frequency component. Giaralis and Spanos [38] have developed a three-stage procedure to generate spectrum-compatible ensembles of seismic records, in which the last stage consists of using the harmonic wavelet transform (HWT) to iteratively improve the matching between the individual artificial accelerogram and the target response spectra. Spanos et al. [39] employed harmonic wavelets in conjunction with the integrated methodology proposed in [38] to generate artificial ground motions compatible with the design response spectrum prescribed by Chinese aseismic regulation. Legrue and Menun [40] have exploited the Daubechies' D20 wavelets to decompose a recorded accelerogram (parent signal) into a number N of sub-signals, which are then multiplied by a set of N uncorrelated time-independent unit-mean random variables with Rayleigh's distribution. It follows that the parent signal constitutes the mean value of the random process so obtained; however, a limited variability is observed for the generated signals (i.e., they tend to be all similar and may not capture the expected level of variability in seismic records).

The latter drawback is common to many methods for simulating artificial accelerograms. To cater to the more significant variability observed in actual earthquake records (which should then be mirrored in the artificial accelerograms), Cacciola and Zentner [41] have proposed a method in which Preumont's procedure for generating samples of fully non-stationary random processes [42] is applied in conjunction with the spectrum-compatible power spectral density (PSD) function previously proposed by Cacciola et al. [43], and a set of random coefficients is introduced to match the mean $\pm$ standard deviation of the target response spectrum. Nakamura et al. [44] proposed a model that employs the discrete wavelet transform (DWT) to generate artificial accelerograms, achieving a target response spectrum through a linear combination of wavelet coefficients derived from observed earthquake motions. Sasaki et al. [45] introduced a model that utilizes the DWT to generate artificial ground motions characterized by time and frequency non-stationarity, employing attenuation models to predict the parameters of their proposed model. Amiri et al. [46] employed the wavelet packet transform to generate artificial ground motions, ensuring compatibility with a target pseudovelocity response spectrum while incorporating time and frequency nonstationarity. In their model, a neural network is used to predict the amplitudes of wavelet packet coefficients. The model's simulations are constrained by a specified target spectrum rather than seismological parameters; however, this makes it challenging to generate ground motions that encompass the complete variability of potential future seismic events.

Yamamoto and Baker [47] have introduced a stochastic ground-motion model that uses the wavelet packet transform to quantify the time and frequency characteristics of the time series. Overall, this comprehensive model requires 13 parameters related to seismological variables such as magnitude, distance, and site conditions, which are determined through a two-stage linear regression analysis. The resulting regression equations are also used to simulate ground motions based on user-defined earthquake scenarios. Thus, in [47], in addition to the predictive nature of the model, wavelets are directly used for simulation of entire time series.

Alternative predictive stochastic models [48–50], based on the spectral representation method (SRM) [51–54], have been proposed to generate fully non-stationary ground motion time histories. Vlachos et al. [48,49] have introduced a stochastic ground motion model, based on regression relationships, developed using a user-specified earthquake scenario description; the model's core is a bimodal analytical fully non-stationary Kanai-Tajimi model [55–57] with physically interpretable parameters. Rezaeian and Der Kiureghian [50] have developed a method for generating a suite of synthetic ground motions tailored to specific earthquake and site characteristics, employing a parameterized stochastic model based on a modulated, filtered white-noise process. In this model [50] the temporal and spectral non-stationarities are separately computed through the modulation of a linear filter's response with time-varying characteristics, considering a white-noise excitation.

Cacciola and Deodatis [58] proposed a SRM-based procedure to generate fully non-stationary and spectrum-compatible multipoint correlated time histories. This method [58] considers the stochastic ground motion as the superposition of: *i*) an evolutionary non-stationary stochastic vector process with amplitude and frequency modulation, representative of local geological and seismological conditions; and *ii*) a non stationary process with only amplitude modulation that adjusts the response spectra of the overall vector process to ensure spectrum compatibility. In [59], Wen et al. proposed a method to generate non-stationary multivariate earthquake accelerograms that match the response spectrum and the characteristics of a parent accelerogram in both the time and frequency domains by combining the wavelet-packet-based approach with the traditional spectral representation method.

Most stochastic generation procedures for accelerograms still assume that phase angles are random variables, independent and uniformly distributed within the range $[0, 2\pi]$. In [60], Ohsaki pointed out that although the Fourier phase angles in recorded accelerograms appeared to be uniformly distributed, they were far from independent. Ohsaki [60] suggested using phase differences (i.e., the differences between Fourier phase angles for consecutive frequencies) to capture information on the non-stationarity of the time history, and showed that although the probability distribution of Fourier phase angles in most real earthquake accelerograms seems uniform, the distribution of phase differences is not uniform and often resembles a normal or normal-like distribution. Hou et al. [61] presented a non-stationary stochastic model for periodic excitation with random phase modulation, accounting for the non-stationarity of the excitation by modelling the phase modulation as a modulated stationary process. In [61], three different types of envelope functions (step, rectangular, and exponential) are considered to study the effects of non-stationarity, including build-up rate, decay, and peak value of the random phase modulation on the system response. Shrikhande and Gupta [62] approached the problem of characterizing phase spectra as a constrained nonlinear programming problem. They modelled the phase curve of earthquake ground motion with a piecewise-linear generic phase curve and added zero-mean Gaussian residual phases to accurately capture the time-domain envelope features of the earthquake ground motion.

In this paper, a novel stochastic model is formulated for the generation of an arbitrary number of "child signals" with non-stationary characteristics similar to those of a chosen "parent record", i.e., a random realization of a zero-mean Gaussian process, representative of the expected seismic action.

The proposed approach employs the circular wavelet transform (CWT) to decompose the recorded accelerogram into complex-valued harmonic wavelets. The artificial signals are then generated by extending the well-known Shinozuka's formula [52,63] to randomize the phases of the contributory wavelets. A new correlation structure is introduced for the random phases to overcome the traditional assumption of statistical independence and provide a higher degree of versatility in the probabilistic representation of the seismic action. Unlike the traditional SRM, the proposed approach: *i*) does not require the definition of the PSD function of seismic acceleration given that it directly pursues the randomization of the parent signal through the proposed generation formula, *ii*) overcomes the traditional assumption of independent random phases uniformly distributed between 0 and 2π. In fact, the main novelty of the proposed procedure lies in the introduction of a new exponential function to account for the statistical correlation among random phases in the generation formula. In this paper, the generic random phase, considered as the discrete value of a two-dimensional mixed time–frequency-domain random field, depends on two seismic parameters, namely: the "strong motion duration" and the "significant frequency bandwidth". The introduction of the proposed correlation structure allows for linking the generation of artificial accelerograms to the expected seismic parameters at a given site, that are easily predictable by using empirical attenuation relationships. The simulation of artificial accelerograms without relying on a target PSD function is not a novelty of the present work. For instance, Chen et al. [8] have recently proposed a method that directly generates pulse-like ground motions in the time domain using the trigonometric series.

In the proposed model, a "circular" version of the Newland's "musical" wavelet has been used as mother wavelet for the randomization of the parent signals. The use of these families of wavelets is particularly suitable for structural dynamic analysis because their Fourier transforms result in box-shaped functions. This property theoretically enables the manipulation of a specific frequency band within a signal without impacting other frequencies. However, some overlapping does occur in practical computation, as it cannot be possible to have filters with an ideal box-shaped spectrum, leading to inevitable energy spillage into adjacent frequency bands in harmonic wavelet transformed signals [64]. The capability of operating within a single frequency band has been exploited by Cecini and Palmeri [22] that have used the wavelet transform method along with the "time of maximum" spectrum concept to develop a systematic approach involving iterative adjustments that target specific frequency bands and time intervals to match a desired earthquake spectrum.

This research highlights the critical role played by the number and size of bands used to partition the frequency domain. In

particular, it is shown that assuming statistically independent random phases and using either a single frequency band or several mono-frequency bands leads to random processes that lose information on the energy distribution in the time or frequency domain, respectively. Instead, adopting an intermediate and conveniently chosen number of frequency bands in conjunction with a suitable time–frequency correlation structure for the random phases can preserve all the desired non-stationary characteristics of the parent signal and achieve an effective trade-off between time and frequency localization. More generally, the choice of how partitioning the frequency domain greatly influences, qualitatively and quantitatively, the outcomes of the simulation. Factors such as analysis objectives, available computational resources, signal characteristics, and required statistics can all influence the decision on the number and width of frequency bands to be adopted.

The paper is organized as follows: Section 2 discusses the key aspects of wavelet analysis for joint time–frequency representation of discrete signals; Section 3 summarizes the novel procedure for randomly generating an arbitrary number of samples with the same non-stationary characteristics as the parent signal; the closed-form expressions for evaluating the statistics of the generated random process are reported in Section 4; finally, in Sections 5 and 6, the influence of the novel correlation structure for defining the wavelets' random phases is highlighted through the application to a generic test signal and to recorded accelerograms, respectively.

2. Wavelet-based representation of discretised signals

A signal is a function of time, but its frequency domain representation can reveal some of its salient features. In an ideal world, engineers and scientists would like to retain as much information as possible in both the time and frequency domains. Unfortunately, this is not possible due to the so-called *Heisenberg's uncertainty principle* (also referred to as the *Heisenberg–Gabor limit*), which states that a signal cannot be simultaneously localised in both the domains (e.g., Ref. [65,66]). The trade-off between time and frequency domain localization is of key importance and can be addressed by wavelet analysis, which involves projecting a given signal onto a convenient set of functions called wavelets, generated by scaling and shifting a mother wavelet [65,67]. Unlike harmonic waves, which are everlasting periodic functions, wavelets are decaying functions. This property allows wavelet analysis not only to reveal the frequency components of signals, as the Fourier transform does, but also to identify where specific frequencies occur in the temporal domain, providing the capability for time localization.

Let's consider a discrete, real-valued signal $F_\ell = f(t_\ell)$, with ℓ=0,1, …, 2N, where $t_\ell = \ell\,\Delta t$ is the generic time instant in which the continuous time signal $f(t)$ has been sampled over the time interval $[0, t_{2N}]$; $\nu_0 = 1/\Delta t$ is the sampling frequency, and $t_{2N} = 2N\,\Delta t$ is the time duration of the signal, known at 2N+1 points. The discrete Fourier Transform (DFT) algorithm can be used to represent the discrete signal in the frequency domain:

$$\left\{\widetilde{F}_0, \widetilde{F}_1, \widetilde{F}_2, \cdots, \widetilde{F}_{2N}\right\}^{\mathrm{T}} = \mathrm{DFT}\left[\{0, F_1 - \overline{F}_1, F_2 - \overline{F}_2, \cdots, 0\}^{\mathrm{T}}\right], \tag{1}$$

where $\widetilde{F}_\ell$ is the DFT value at the ℓth discrete frequency $\omega_\ell = \ell\ \Delta\omega$, $\Delta\omega = 2\pi/t_{2N}$ being the discretisation step in the frequency domain; the superscripted T means transpose; $\overline{F}_\ell$ is the ℓth linear-trend value in the time domain, so defined:

$$\overline{F}_\ell = F_0 + \frac{F_{2N} - F_0}{2N}\ell\ ; \tag{2}$$

and, for $1 \le \ell \le N$, $\widetilde{F}_\ell = \widetilde{F}^*_{2N+1-\ell}$, where the superscripted asterisk means complex conjugate; furthermore, $\widetilde{F}_0$ is real-valued and ω_N=N $\Delta\omega$ is the *Nyquist frequency*.

Different formulations are available to perform the DFT; without loss of generality, the following expression has been adopted in the present work:

$$\widetilde{F}_\ell = \sum_{s=0}^{2N} (F_s - \overline{F}_s)\exp\left(-i2\pi\frac{\ell s}{2N+1}\right), \tag{3}$$

in which $i = \sqrt{-1}$ is the imaginary unit.

The frequency range $[0, \omega_N]$ can be arbitrary partitioned in M frequency bands $[\omega_{m_j},\ \omega_{n_j}]$, with $j \le M$ and $1 \le M \le N$; furthermore, $m_1 = 0,\ n_M = N$; and, for $1 \le j \le M$, $n_j = m_{j+1}$, so that jth and (j+1)th frequency bands are adjacent to each other, without any overlapping or gaps. Bandwidth and central circular frequency of the jth band are given by:

$$B_j = b_j\Delta\omega; \tag{4}$$

$$\overline{\omega}_j = \frac{m_j + n_j}{2}\Delta\omega, \tag{5}$$

in which $b_j = n_j - m_j$. In line with the assumed partitioning of the frequency domain, the generic complex-valued circular wavelet in the discretised time domain can be defined as:

$$\Psi_{j,k,\ell} = \frac{1}{b_j}\sum_{s=m_j}^{n_j-1}\exp\left[i\pi(2s+1)\left(\frac{\ell}{2N} - \frac{k}{b_j}\right)\right], \tag{6}$$

where $k = 0,\ 1,\ \ldots,\ b_j - 1$ and ℓ=0,1, …, 2 N are two time indexes, defining the time instants at which the wavelet $\Psi_{j,k,\ell}$ is centered $\left(\tau_{j,k} = k\ t_{2N}/b_j\right)$ and evaluated (t_ℓ), respectively. Importantly, the larger b_j, i.e., the wider the jth frequency band, the larger the number of wavelets $\Psi_{j,0,\ell}, \Psi_{j,1,\ell}, \cdots, \Psi_{j,b_j-1,\ell}$ belonging to it, the more precise the time localisation of the energy can be achieved in that frequency band.

For the given discrete signal F_ℓ, the generic complex-valued wavelet coefficient can be calculated as:

$$\widehat{a}_{j,k} = \frac{b_j}{2N}\sum_{\ell=0}^{2N}(F_\ell - \overline{F}_\ell)\Psi^*_{j,k,\ell}\ , \tag{7}$$

and the signal can be reconstructed as:

$$\widehat{F}_\ell = \overline{F}_\ell + 2\mathrm{Re}\left[\sum_{j=1}^{M}\sum_{k=0}^{b_j-1}\widehat{a}_{j,k}\Psi_{j,k,\ell}\right], \tag{8}$$

where Re[·] returns the real part of the complex-valued expression within square brackets. It is worth mentioning here that, independently of the band-partitioning of the frequency domain, $N = \sum_{j=1}^{M} b_j$ is the number of wavelets contributing to the double summation in the right-hand side (rhs) of Eq.(8).

Alternatively, the reconstruction formula of Eq. (8) can be expressed as:

$$\widehat{F}_\ell = \overline{F}_\ell + 2\sum_{j=1}^{M}\frac{1}{b_j}\sum_{k=0}^{b_j-1}\left|\widehat{a}_{j,k}\right|\sum_{s=m_j}^{n_j-1}\cos\left[\pi(2s+1)\left(\frac{\ell}{2N}-\frac{k}{b_j}\right)+\widehat{\theta}_{j,k}\right], \tag{9}$$

where $\widehat{a}_{j,k} = \left|\widehat{a}_{j,k}\right|e^{i\widehat{\theta}_{j,k}}$ is the exponential form of the generic wavelet coefficient $\widehat{a}_{j,k}$; that is, $\widehat{\theta}_{j,k} = \angle\widehat{a}_{j,k}$ and $|\widehat{a}_{j,k}|$ are the phase angle and modulus of $\widehat{a}_{j,k}$, respectively.

A special case occurs for M=N i.e., when there are N frequency bands $[\omega_j,\omega_{j+1}]$, all with the same bandwidth $B_j = \Delta\omega$, i.e., $b_1 = b_2 = \ldots = b_N = 1$. Accordingly, there is only one wavelet $\Psi_{j,0,\ell}$ and one wavelet coefficient $\widehat{a}_{j,0}$ for each frequency band (i.e., no time localisation occurs in any of the M "monochromatic" frequency bands), and Eq.(9) can be rewritten as:

$$\widehat{F}_\ell = \overline{F}_\ell + 2\sum_{j=1}^{N}\left|\widehat{a}_{j,0}\right|\cos\left(\overline{\omega}_j t_\ell + \widehat{\theta}_{j,0}\right), \tag{10}$$

with $\overline{\omega}_j = \frac{1}{2}\left(\omega_j + \omega_{j+1}\right)$, which particularises Eq. (5).

The opposite situation occurs for $b_j = N$. In this case, there is only one frequency band (M=1) and the particularization of Eq. (9) leads to:

$$\widehat{F}_\ell = \overline{F}_\ell + \frac{2}{N}\sum_{k=0}^{N-1}\left|\widehat{a}_{1,k}\right|\sum_{s=0}^{N-1}\cos\left[\pi(2s+1)\left(\frac{\ell}{2N}-\frac{k}{N}\right)+\widehat{\theta}_{1,k}\right] \tag{11}$$

In this case: *i*) a perfect localisation is achieved in the time domain; *ii*) no localization is possible in the frequency domain, where the energy of the wavelet is spread nearly uniformly over the frequency range $[0,\omega_N]$.

Note that increasing the number M of the frequency bands results in an improved resolution in the frequency domain, i.e., a more detailed representation of the frequency content, however, the larger M, less detailed is the representation of the signal in the time domain. Furthermore, the wavelet transform becomes DFT when harmonic wavelet expansion, with one coefficient per scale, is taken.

3. Proposed randomisation procedure

Let $F(t)$ be a zero-mean, stationary Gaussian process, fully defined in the frequency domain by the power spectral density (PSD) function $S_F(\omega)$. A generic realisation of the random process $F(t)$ can be obtained using the so-called *Shinozuka's formula* [52,63], which requires the following steps:

1. choose a " cut-off " frequency ω_N such that (for the purposes of the analysis being carried out) the energy of the random process can be neglected for $\omega > \omega_N$;
2. divide the frequency range of interest $[0,\omega_N]$ into a "large number" N of intervals of equal width $\Delta\omega = \omega_N/N$;
3. calculate the value of the PSD function at the central frequency of each interval $\Delta\omega$, that is $S_j = S_F\left(\overline{\omega}_j\right)$, width $\overline{\omega}_j = \left(j - \frac{1}{2}\right)\Delta\omega$ and $j = 1,2,\ldots,N$;
4. generate a set of N statistically independent random variables, $\left\{\phi_1^{(r)},\phi_2^{(r)},\cdots,\phi_N^{(r)}\right\}$, uniformly distributed over the range $[-\pi,\pi]$;
5. generate the rth sample of the random process through a superposition of N harmonic functions with random phases:

$$F^{(r)}(t_\ell) = 2\sum_{j=1}^{N} \sqrt{S_j\,\Delta\omega}\cos\left(\overline{\omega}_j\, t_\ell + \phi_j^{(r)}\right), \tag{12}$$

where t_ℓ is the generic time instant at which the sample is evaluated;

6. repeat steps 4 and 5 for $r = 1, 2, 3, \cdots$, until enough samples of the random process have been obtained.

It should be noted that: *i*) the number N of harmonic functions must be large enough for the central limit theorem to apply (e.g., [68]); *ii*) the generated sample $F^{(r)}(t)$ is periodic, of period $\overline{T}_1 = 2\pi/\overline{\omega}_1 = 4\pi/\Delta\omega$; *iii*) using *Euler's formula*, Eq. (12) is equivalent to:

$$F^{(r)}(t_\ell) = 2\mathrm{Re}\left[\sum_{j=1}^{N} C_{j,\ell}\,\exp\left(i\,\phi_j^{(r)}\right)\right], \tag{13}$$

where the complex-valued coefficients $C_{j,\ell} = \sqrt{S_j\,\Delta\omega}\,\exp\left(i\,\overline{\omega}_j\, t_\ell\right)$ are sample-independent, so they need to be calculated only once, while the sample-to-sample variability is achieved through the generation of the random phases $\phi_j^{(r)}$. Shinozuka's formula of Eq. (12) is remarkably similar to Eq. (10), which particularises the wavelet-based reconstruction of a discrete signal when the number M of frequency bands is the same as the number N of wavelets being used [69,17]. This suggests the possibility of using random phases to randomise the contributions of the harmonic functions appearing in the circular wavelets used to reconstruct a discrete signal. Accordingly, Eq. (9) can be randomised as:

$$F_\ell^{(r)} = F^{(r)}(t_\ell) = 2\sum_{j=1}^{M}\frac{1}{b_j}\sum_{k=0}^{b_j-1}\left|\widehat{a}_{j,k}\right|\sum_{s=m_j}^{n_j-1}\cos\left[\pi(2s+1)\left(\frac{\ell}{2N}-\frac{k}{b_j}\right)+\widehat{\theta}_{j,k}+\phi_{j,k}^{(r)}\right], \tag{14}$$

in which, without loss of generality, a zero trend line has been assumed (i.e., consistent with the assumption of zero mean random process, $\overline{F}_\ell = 0$), and $\boldsymbol{\phi}^{(r)} = \left\{\phi_{1,0}^{(r)},\ \ldots,\phi_{j,k}^{(r)},\ \ldots,\phi_{M,b_M-1}^{(r)}\right\}^{\mathrm{T}}$ is the N-dimensional array collecting the rth realisations of random phases uniformly distributed over the range $[-\pi, \pi]$. Noteworthily: *i*) if all the random phases are set to zero, i.e., if $\boldsymbol{\phi}^{(r)} = \{0, \ldots, 0, \ldots, 0\}^{\mathrm{T}}$, the rth realisation of the random signal $F_\ell^{(r)}$ of Eq. (14) coincides with the discrete signal $\widehat{F}_\ell^{(r)}$, deterministically reconstructed via Eq. (9); *ii*) the generic element $\phi_{j,k}^{(r)}$ of the random vector $\boldsymbol{\phi}^{(r)}$ represents the random rotation of the circular wavelet $\Psi_{j,k,\ell}$ of Eq. (6), whose real part is the (j, k)th contribution to the random realization $F_\ell^{(r)}$. In this respect, the role of $\widehat{\theta}_{j,k}$ is similar to that of $\phi_{j,k}$; however, while the angle $\widehat{\theta}_{j,k}$ is deterministically required to achieve the reconstruction of a given signal, the angle $\phi_{j,k}$ acts on the same (j, k)th wavelet to randomise its contribution.

It follows that the generation formula of Eq. (14) can be expressed in the equivalent form:

$$F_\ell^{(r)} = 2\,\mathrm{Re}\left[\sum_{j=1}^{M}\sum_{k=0}^{b_j-1}\widehat{C}_{j,k,\ell}\,\exp\left(i\,\phi_{j,k}^{(r)}\right)\right], \tag{15}$$

in which the generic coefficient $\widehat{C}_{j,k,\ell}$ is sample-independent and defined as:

$$\widehat{C}_{j,k,\ell} = \widehat{a}_{j,k}\,\Psi_{j,k,\ell} = \frac{\widehat{a}_{j,k}}{b_j}\sum_{s=m_j}^{n_j-1}\exp\left[i\,\pi\,(2s+1)\left(\frac{\ell}{2N}-\frac{k}{b_j}\right)\right] = \widehat{C}_{j,k,\ell}^{\,\prime} + i\,\widehat{C}_{j,k,\ell}^{\,\prime\prime}, \tag{16}$$

where $\widehat{C}_{j,k,\ell}^{\,\prime} = \mathrm{Re}\left[\widehat{C}_{j,k,\ell}\right]$ and $\widehat{C}_{j,k,\ell}^{\,\prime\prime} = \mathrm{Im}\left[\widehat{C}_{j,k,\ell}\right]$ are its real part and imaginary part, respectively.

The comparison between Eqs. (13) and (15) reveals that the proposed wavelet-based generation formula coincides with the conventional Shinozuka's formula in the special case where M=N, which implies $b_1 = b_2 = \ldots = b_M = 1$ (i.e., each frequency band consists of a single discrete frequency), $m_j = j$-1 and $n_j = j$. In this case $k = 0$ and there is no time localization since there is only one wavelet in each monochromatic frequency band. As a consequence, no information is preserved in the time domain, meaning that the child signals generated in this way represent samples of a stationary random process with an expected linear trend in the cumulative intensity function. The sample-independent coefficients are given by:

$$\widehat{C}_{j,0,\ell} = \widehat{C}_{j,\ell} = \widehat{a}_{j,0}\,\exp\left[i\,\pi\,\frac{(2j-1)\,\ell}{2N}\right]. \tag{17}$$

Importantly, in the Shinozuka's formula, the random phases ϕ_j are assumed to be statistically independent; that is, for $j \neq J$ and any pair of exponents a and b:

$$\mathbb{E}\left[\phi_j^a\,\phi_J^b\right] = \mathbb{E}\left[\phi_j^a\right]\mathbb{E}\left[\phi_J^b\right], \tag{18}$$

where $\mathbb{E}\,[\cdot]$ is the expectation operator.

Furthermore, mean value and variance of the generic random phase are:

$$\mu_\phi = \mathbb{E}\left[\phi_j\right] = 0\,; \tag{19}$$

$$\sigma_\phi^2 = \mathbb{E}\left[\phi_j^2\right] = \pi^2 \big/ 3\,. \tag{20}$$

On the contrary, in the proposed generation formula, an arbitrary correlation structure can be adopted for the random phases $\phi_{j,k}$. The implications of accounting for the correlation between the random phases are explored in the following sections.

4. Statistics of the generated random process

In this section, the statistical properties of the generation formula of Eq. (15) are investigated in detail.

4.1. Mean value

The application of the expectation operator to both sides of the Eq. (15) yields:

$$\mu_{F(\ell)} = \mathbb{E}[F(\ell)\,] = 2\sum_{j=1}^{M}\sum_{k=0}^{b_j-1}\mathbb{E}\left[\widehat{C}'_{j,k,\ell}\cos\left(\phi_{j,k}\right) - \widehat{C}''_{j,k,\ell}\sin\left(\phi_{j,k}\right)\right] = 0, \tag{21}$$

as $\mathbb{E}\left[\cos\left(\phi_{j,k}\right)\right] = 0$ and $\mathbb{E}\left[\sin\left(\phi_{j,k}\right)\right] = 0$. It follows that, similarly to the Shinozuka's formula, the generated random process $F(\ell) = F(t_\ell)$ has zero mean.

4.2. Correlation function

According to the mathematical definition of the second-order correlation function, for the proposed generation formula, one gets:

$$\begin{aligned} R_{FF(\ell,L)} &= \mathbb{E}[F_\ell\, F_L] = 4\sum_{j=1}^{M}\sum_{k=0}^{b_j-1}\sum_{J=1}^{M}\sum_{K=0}^{b_J-1}\mathbb{E}\left[\left\{\widehat{C}'_{j,k,\ell}\cos\left(\phi_{j,k}\right) - \widehat{C}''_{j,k,\ell}\sin\left(\phi_{j,k}\right)\right\}\left\{\widehat{C}'_{J,K,L}\cos\left(\phi_{J,K}\right) - \widehat{C}''_{J,K,L}\sin\left(\phi_{J,K}\right)\right\}\right] \\ &= 4\sum_{j=1}^{M}\sum_{k=0}^{b_j-1}\sum_{J=1}^{M}\sum_{K=0}^{b_J-1}\left\{\widehat{C}'_{j,k,\ell}\;\widehat{C}'_{J,K,L}\,\sigma_{\mathrm{cc}(j,k,J,K)} + \widehat{C}''_{j,k,\ell}\;\widehat{C}''_{J,K,L}\,\sigma_{\mathrm{ss}(j,k,J,K)}\right\}, \end{aligned} \tag{22}$$

where $\sigma_{\mathrm{cc}(j,k,J,K)} = \mathbb{E}\left[\cos\left(\phi_{j,k}\right)\cos\left(\phi_{J,K}\right)\right]$ and $\sigma_{\mathrm{ss}(j,k,J,K)} = \mathbb{E}\left[\sin\left(\phi_{j,k}\right)\sin\left(\phi_{J,K}\right)\right]$ are the covariances of the cosine and sine of the random phases $\phi_{j,k}$ and $\phi_{J,K}$, respectively. The variance of the generated random process can be obtained by setting $\ell = L$ in Eq. (22); that is:

$$\sigma_{F(\ell)}^2 = \mathbb{E}\left[F_\ell^2\right] = R_{FF(\ell,\ell)}\,. \tag{23}$$

Furthermore, in the last line of Eq. (22): *i*) the condition $\mathbb{E}\left[\cos\left(\phi_{j,k}\right)\sin\left(\phi_{J,K}\right)\right] = 0$ has been used to simplify the final expression (this outcome arises from the mathematical observation that the expected value of the product of the terms enclosed within the square brackets yields an odd function within a symmetric interval; hence, it results in a zero outcome); *ii*) the covariances σ_{cc} and σ_{ss} appearing in Eq. (22) only depend on the linear correlation coefficient $\rho_{\phi\phi(j,k,J,K)}$ between the relevant random phases; that is:

$$\sigma_{\mathrm{cc}(j,k,J,K)} = \sigma_{\mathrm{cc}}\left(\rho_{\phi\phi(j,k,J,K)}\right); \tag{24a}$$

$$\sigma_{\mathrm{ss}(j,k,J,K)} = \sigma_{\mathrm{ss}}\left(\rho_{\phi\phi(j,k,J,K)}\right). \tag{24b}$$

The calculation of these covariances can be performed once the vector collecting the random phases, $\boldsymbol{\phi}$, is conveniently expressed through the following transformation of variables:

$$\boldsymbol{\phi} = \Phi(\boldsymbol{u}), \tag{25}$$

where $\boldsymbol{u} = \{u_1, \ldots, u_i, \ldots, u_N\}^{\mathrm{T}}$ is an N-dimensional vector of zero-mean, Gaussian variables with unitary variance, i.e., $\sigma_{u(i)} = \mathbb{E}\left[u_i^2\right] = 1$; and the transformation function is:

$$\Phi(u) = \pi\,\mathrm{erf}\left(\frac{u}{\sqrt{2}}\right), \tag{26}$$

in which erf(·) is the error function; furthermore, a given pair of frequency index j and time index k is mapped onto the position i of the corresponding random variable u_i through the following bijective expression:

$$i = 1 + k + \sum_{h=1}^{j} b_h\left(1 - \delta_{j,h}\right), \tag{27}$$

in which $\delta_{j,h}$ is the Kronecker's delta, such that $\delta_{j,h} = 1$ if and only if $j = k$.

The covariances of Eqs. (24) can be computed through the following double integrals:

$$\sigma_{cc(i,I)} = \int_{-\infty}^{+\infty}\int_{-\infty}^{+\infty} \cos[\Phi(u_i)]\cos[\Phi(u_I)]\,\mathrm{p}_{uu(i,I)}(u_i,u_I)\mathrm{d}u_i\,\mathrm{d}u_I; \tag{28a}$$

$$\sigma_{ss(i,I)} = \int_{-\infty}^{+\infty}\int_{-\infty}^{+\infty} \sin[\Phi(u_i)]\sin[\Phi(u_I)]\,\mathrm{p}_{uu(i,I)}(u_i,u_I)\mathrm{d}u_i\,\mathrm{d}u_I, \tag{28b}$$

where the indexes i and I are associated with the frequency-time pairs $\{j, k\}$ and $\{J,K\}$, respectively; $\mathrm{p}_{uu(i,I)}(u_i,u_I)$ is the bivariate PDF (probability density function) of the auxiliary random variables u_i and u_I:

$$\mathrm{p}_{uu(i,I)}(u_i,u_I) = \frac{1}{2\pi\sqrt{1-\rho_{uu(i,I)}^2}}\exp\left[-\frac{u_i^2 - 2\rho_{uu(i,I)}u_iu_I + u_I^2}{2\left(1-\rho_{uu(i,I)}^2\right)}\right], \tag{29}$$

in which the auxiliary correlation coefficient $\rho_{uu(i,I)}$ is a function of the linear correlation coefficient between the corresponding random phases [70]:

$$\rho_{uu(i,I)} = 2\sin\left(\frac{\pi}{6}\rho_{\phi\phi(j,k,J,K)}\right). \tag{30}$$

For fully correlated random phases, i.e., for $\rho_{uu(i,I)} = 1$, the double integrals of Eqs. (28) can be evaluated in closed form, and one gets $\sigma_{cc}(1) = \sigma_{ss}(1) = 1/2$ for any choice of the indexes i and I.

For statistically independent random phases, i.e., for $\rho_{uu(i,I)} = \delta_{i,I}$ the covariances of their cosine and sine functions are zero for $i \neq I$, that is: $\sigma_{cc}(\delta_{i,I}) = \sigma_{ss}(\delta_{i,I}) = (1/2)\delta_{i,I}$. Accordingly, Eqs. (22) and (23) simplify as:

$$R_{FF(\ell,L)} = 2\sum_{j=1}^{M}\sum_{k=0}^{b_j-1}\left\{\widehat{C}'_{j,k,\ell}\,\widehat{C}'_{j,k,L} + \widehat{C}''_{j,k,\ell}\,\widehat{C}''_{j,k,L}\right\}; \tag{31}$$

$$\sigma^2_{F(\ell)} = 2\sum_{j=1}^{M}\sum_{k=0}^{b_j-1}\left|\widehat{C}_{j,k,\ell}\right|^2. \tag{32}$$

For the general case of partially correlated random phases, i.e., for $0 < \rho_{\phi\phi(j,k,J,K)} < 1$, the double integrals can be computed numerically. This has been done for $\rho_{\phi\phi(j,k,J,K)} = 0.02, 0.04, \cdots, 0.98$. The data points so obtained have then been best-fitted with the following polynomial expressions:

$$\sigma_{cc}(\rho) \approx 0.280971\,\rho^2 + 0.098309\rho^3 + 0.12072\rho^7; \tag{33}$$

$$\sigma_{ss}(\rho) \approx 0.224567\,\rho + 0.16018\rho^3 + 0.115252\rho^7. \tag{34}$$

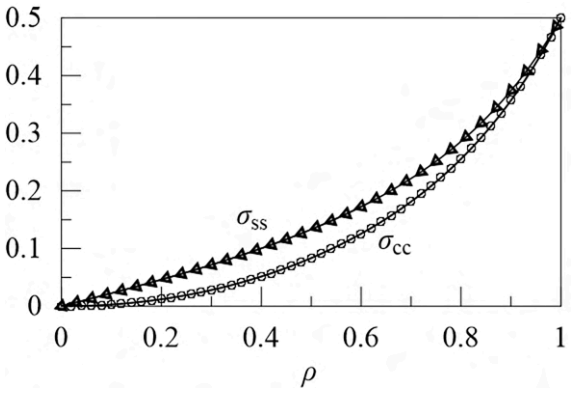

Fig. 1. Covariance of the harmonic functions of uniformly distributed random phases with linear correlation coefficient ρ: circle ○, $\sigma_{cc}(\rho)$; triangle △, $\sigma_{ss}(\rho)$.

The two best-fit functions of Eqs. (33) and (34) are plotted with solid lines in Fig. 1 along with the data points (empty circles and triangles) used to determine them.

From the above derivation, it appears that the random process F_ℓ, generated through the circular wavelets, has a correlation function that depends on: *i*) the partitioning of the frequency range $[0, \omega_N]$ in the M frequency bands $B_1, \ldots, B_M$; *ii*) the correlation structure assumed for the random phases $\phi_{j,k}$. The implications of different choices will be investigated in the next sections with reference to an amplitude-modulated chirp (AMC, in Section 5) and to recorded accelerograms (Section 6).

5. Numerical validation

In order to validate the formulae derived in the previous section, let's consider the test signal defined as:

$$f(t) \;=\; 3 - t^{3/2} + 2\sin^2(\pi t)\cos\left[7\pi\left(t + t^3\right)\right]; \tag{35}$$

that is, an amplitude-modulated chirp (AMC) superimposed with a non-linear trend (NLT) function.

The time duration is $t_{2N} = 2$ s and the sampling frequency is $\nu_0 = 100$ Hz, meaning that the discretised signal consists of $2N + 1 = \nu_0\, t_{2N} + 1 = 201$ points. A time step $\Delta t = 0.01$ s has been adopted. The number of the discrete non-zero frequencies is N=100, the Nyquist frequency is $\omega_N = 314.2$ rad/s and the frequency step is $\omega_N / N = \Delta\omega = 3.142$ rad/s. The linear trend defined by the boundary values $f(0) = 3$ and $f(t_{2N}) = 0.171573$ has been removed from the signal (see Eqs. (1) and (2)). In the following, the de-trended signal thus obtained is referred to as the "parent signal", $\bar{f}(t)$, such that $\bar{f}(0) = 0$ and $\bar{f}(t_{2N}) = 0$. The frequency range of interest, $[0, \omega_N = 314.16$ rad/s], has been partitioned in seven frequency bands (i.e. M=7) of nearly uniform bandwidth, i.e., $B_j = 43.98$ rad/s for $j \leq 7$ with the exceptions of $B_2 = B_6 = 47.12$ rad/s. The number of circular wavelets in the frequency bands is $b_j = 14$ for $j = 1, 3, 4, 5, 7$ and $b_j = 15$ for $j = 2, 6$. One hundred is the total number of wavelets, i.e, $b_1 + b_2 + \cdots + b_7 = N = 100$.

Three correlation structures have been assumed for the random phases in the N-dimensional vector $\boldsymbol{\phi}$, namely:

i. "uncorrelated" (UC), so that $\rho_{\phi\phi(j,k,J,K)} = 0$ if the random phases $\phi_{j,k}$ and $\phi_{J,K}$ are different from each other;
ii. "partially correlated" (PC), in which, among all the possible choices, the linear correlation coefficient for a generic pair of random phases has been assumed as:

$$\rho_{\phi\phi(j,k,J,K)} = \left(1 - \frac{|J-j|}{M-1}\right)\left(1 - \left|\frac{K}{b_J - 1} - \frac{k}{b_j - 1}\right|\right), \tag{36}$$

meaning that $\rho_{\phi\phi(j,k,J,K)} = 1$ only for $\{j, k\} = \{J, K\}$ and $\rho_{\phi\phi(j,k,J,K)} = 0$ when the corresponding wavelets $\Psi_{j,k,\ell}$ and $\Psi_{J,K,\ell}$ belong to frequency bands at the opposite sides of the frequency range (e.g., $j = 1$ and $J = M$) or are centered at the opposite sides of the time interval (e.g., $k = 0$ and $K = b_J - 1$);
iii. "fully correlated" (FC), so that $\rho_{\phi\phi(j,k,J,K)} = 1$ for any pair of random phases $\phi_{j,k}$ and $\phi_{J,K}$, meaning that their rth realisations coincide to each other, i.e., $\phi_{j,k}^{(r)} = \phi_{J,K}^{(r)}$.

The top row of Fig. 2 provides a visual representation of the elements of the $N \times N$ covariance matrix of the random phases, $\sum_{\phi\,\phi} = \mathbb{E}\left[\boldsymbol{\phi} \cdot \boldsymbol{\phi}^{\mathrm{T}}\right]$, in which the dot sign $(\cdot)$ stands for the row-by-column matrix product. Its (i, I)th element is given by:

$$\sum\nolimits_{\phi\phi(i,I)} = \frac{\pi^2}{3}\rho_{\phi\phi(j,k,J,K)} \tag{37}$$

where Eq. (27) establishes the relationship between the index triples $\{i, j, k\}$ and $\{I, J, K\}$. The color scheme used for the matrix plots of Fig. 2(a) to 2(c) ranges from "white" when $\Sigma_{\phi\phi(i,I)} = 0$ (i.e., the random phases $\phi_{j,k}$ and $\phi_{J,K}$ are statistically independent) to "black" when $\sum_{\phi\phi(i,I)} = \pi^2/3 = \sigma_\phi^2$ (i.e., the random phases $\phi_{j,k}$ and $\phi_{J,K}$ are fully correlated). Accordingly:

- $\boldsymbol{\Sigma}_{\phi\phi}$ is a diagonal matrix in Fig. 2(a), corresponding to the case of UC random phases;
- $\boldsymbol{\Sigma}_{\phi\phi}$ is a constant matrix in Fig. 2(c), corresponding to the case of FC random phases;
- the covariance matrix $\boldsymbol{\Sigma}_{\phi\phi}$ of the PC model (Eq. (36)) appears partitioned in $M \times M$ blocks of dimensions $b_i \times b_I$ (see Fig. 2(b)). The closer the block to the main diagonal of the covariance matrix, the darker the shades of its elements; in fact, the closer the frequency bands j and J, the higher the correlation between the corresponding random phases (for instance, the blocks $(1, M)$ and $(M, 1)$ are completely white as they are associated with the most distant frequency bands). Furthermore, within each block, the closer the element to the main diagonal of the block, the darker the shades; in fact, the closer the time centres of the wavelets $\Psi_{j,k,\ell}$ and $\Psi_{J,K,\ell}$ (proportional to the time indexes k and K), the higher the correlation between the corresponding random phases.

It is worth emphasising here that the cases of UC and FC random phases are limiting models which maximise and minimise the variability of the generated random samples, respectively. On the other hand, the PC case of Eq. (36) is only one of the many intermediate models that can be assumed for the random phases.

The middle row of Fig. 2 illustrates the effects of different covariance matrices $\boldsymbol{\Sigma}_{\phi\phi}$ on the sample-to-sample variability of the

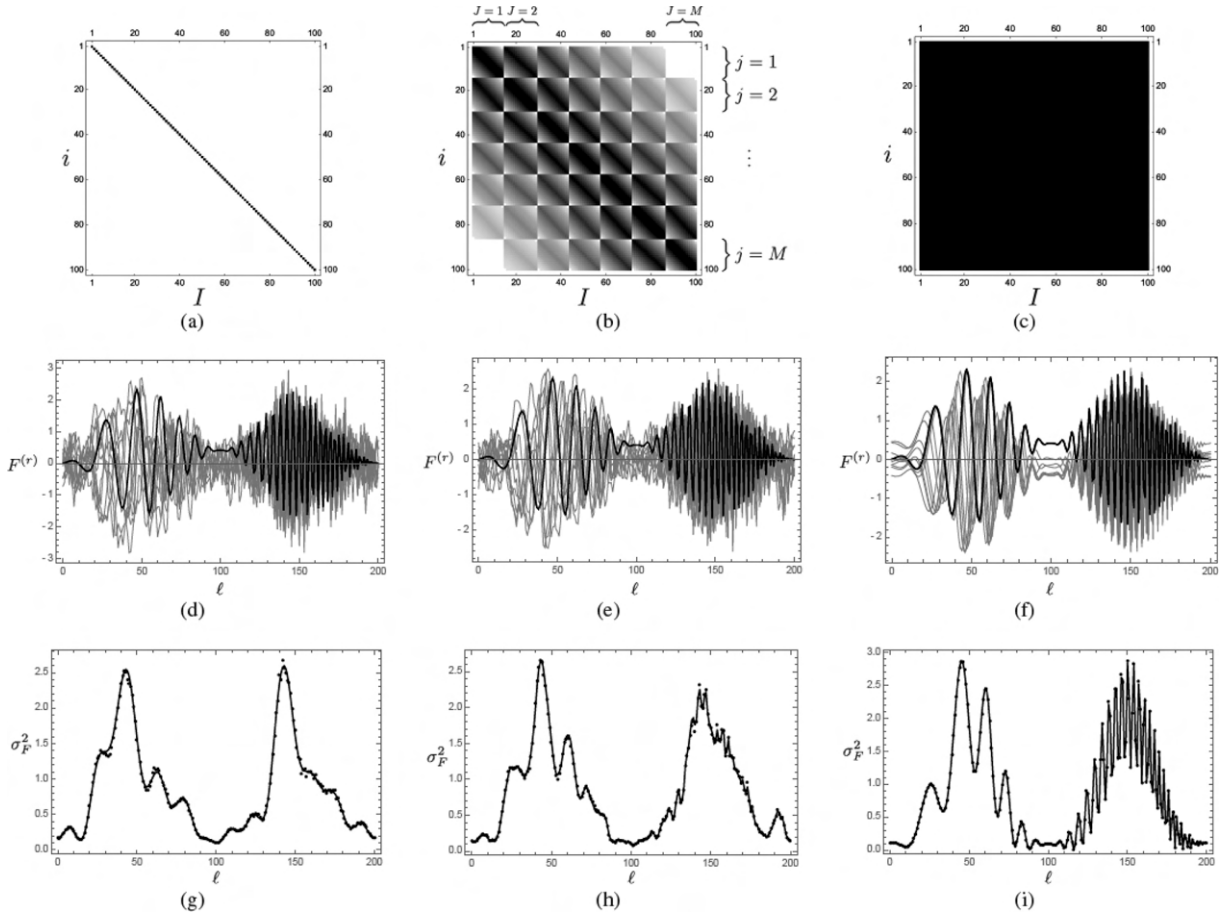

Fig. 2. Top row, matrix plots of the covariance matrix $\mathbf{\Sigma}_{\phi\phi}$ when the random phases $\phi_{j,k}^{(r)}$ are uncorrelated (UC, Fig. 2(a), left column), partially correlated (PC, Fig. 2(b), middle column) and fully correlated (FC, Fig. 2(c), right column). Middle row, generated samples $F_\ell^{(r)}$ for the three correlation models (thin lines in Fig. 2(d) to 2(f)), compared against the parent signal (thick lines). Bottom row, time-dependent variance $\sigma_{F(\ell)}^2$ evaluated using the proposed formulae (solid lines, Eqs. (22)-(23)) and (32)) and MCS (dots).

generated samples. Specifically, ten samples $F_\ell^{(r)}$ (with $r = 1,2,\ldots,10$) have been generated through Eq. (15) for each of the three correlation models (thin lines) and compared against the parent signal $\bar{f}(t_\ell)$ (thick lines). The generated samples of Fig. 2(d) appear much more irregular than the parent signal, although its signature features in both the time and frequency domains are preserved, i.e., increasing number of up-crossing of the time axis and peak amplitudes at about $\ell = 45$ and $\ell = 145$. Similar considerations can be made for the ten samples of Fig. 2(e), although, from a visual inspection, their variability appears less pronounced than in the previous case. Finally, all the generated samples of the FC case (Fig. 2(f)) show the same regular chirp-like oscillations as the parent signal.

An important consideration here is that, given the generation formulae (Eqs. (14) and (15)), the parent signal $\bar{f}(t_\ell)$ represents a possible realisation for all the three random processes obtained for the UC, PC and FC model (i.e., the realisation, when all the random phases are equal to zero, is a non-null event in all these models); however, "qualitatively", the parent signal resembles the generic samples of the FC model more than the samples of the other two cases.

The bottom row of Fig. 2 demonstrates the accuracy of Eqs. (22) and (23) (general randomisation case) and Eqs. (31) and (32) (UC random phases only) in evaluating the variance of the generated random process, $\sigma_{F(\ell)}^2$, as the prediction of these formulae (solid lines) are compared against the outcomes of an MCS (Monte Carlo simulation) carried out with 1000 samples (dots). In all cases, an excellent agreement is observed.

It is worth noting here that the variance of the signal in the case of FC random phases (Fig. 2(i)) shows fluctuations that match deterministically the chirp-like oscillations of the parent signal. These fluctuations are much less visible in the PC case (Fig. 2(h)) and virtually disappear in the UC case (Fig. 2(g)), highlighting how the correlation model adopted for the random phases $\phi_{j,k}$ affect the generated random process.

6. Numerical applications to seismic signals

In this section, before investigating the effects of different modelling choices in the wavelet-based stochastic generation of seismic accelerograms, a new exponential function is introduced to account for the statistical correlation between the random phases in the proposed generation formula. Additionally, a brief overview of some commonly used engineering measures for earthquake ground motions is presented, as these quantities are used subsequently to investigate the effects of different randomization choices on the stochastic generation of accelerograms.

6.1. Engineering representation of seismic action

The analysis of strong ground motions recorded during seismic events plays a crucial role in earthquake engineering. Often, the characteristics of the seismic ground motion can be conveniently quantified in terms of a range of parameters directly extracted from the time history of the ground acceleration, $\ddot{u}_g(t)$.

6.1.1. Arias intensity and Husid's function

The *Arias intensity*, I_A, is one of the most common measures of seismic intensity [5]. Dimensionally equivalent to a velocity, this seismic parameter captures the destructiveness potential of an earthquake as the integral of the square of the ground acceleration:

$$I_A = \frac{\pi}{2g}\int_0^{T_g}\left(\ddot{u}_g(t)\right)^2 \mathrm{d}t\,, \tag{38}$$

where g is the acceleration of gravity and $[0, T_g]$ is the time interval in which the ground motion occurs. The cumulative distribution of the seismic signal, normalised with respect to the Arias intensity, is known as *Husid's function* [71] and can be expressed as:

$$J(t) = \frac{\pi/(2g)}{I_A}\int_0^{t}\left(\ddot{u}_g(s)\right)^2 \mathrm{d}s\,, \tag{39}$$

with $0 \le t \le T_g$ and $J(T_g) = 1$.

The Husid's function can be used to determine the accelerogram's "strong motion duration", i.e., the portion of the accelerogram which is more likely to cause damage to the built environment. Several definitions have been proposed in the literature [72]. The most

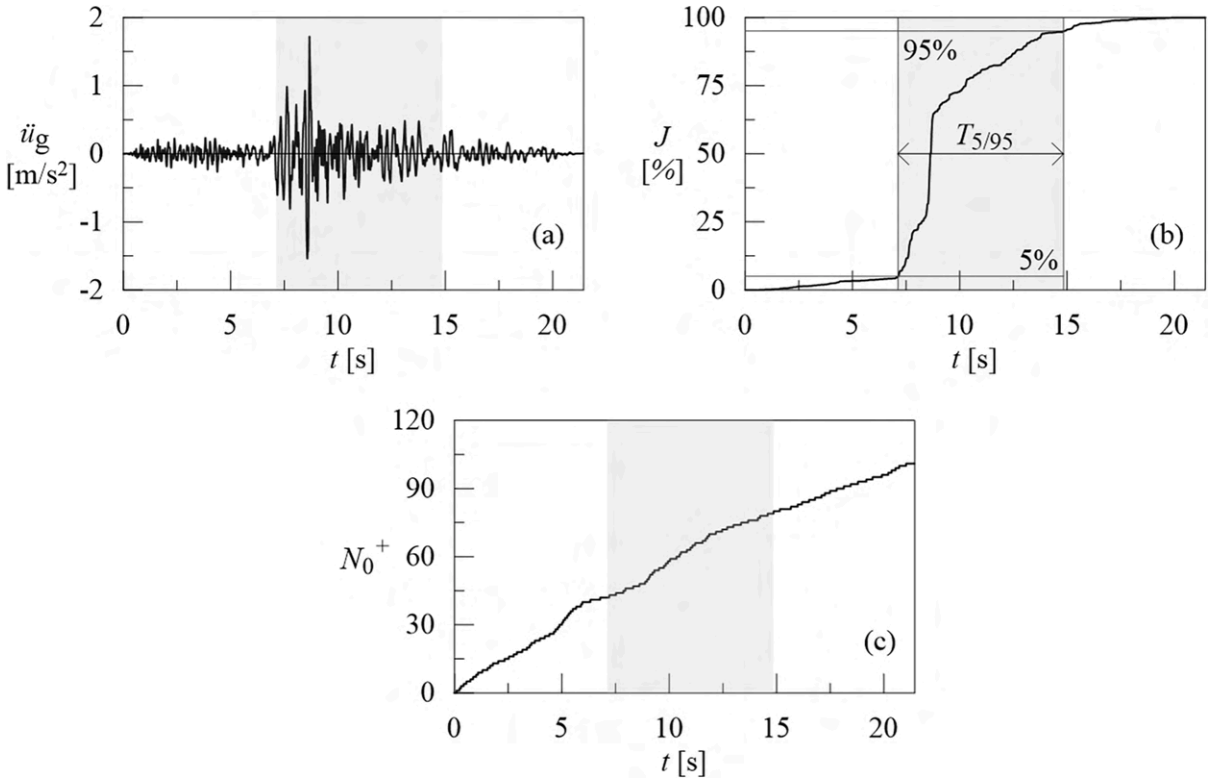

Fig. 3. Time history of illustrative accelerogram recorded during the 1983 Trinidad offshore earthquake (a); normalised cumulative intensity and strong-motion duration (b); cumulative zero-level up-crossings function (c).

commonly used is the "significant duration" [73], which is the time interval over which a certain percentage of the Arias intensity cumulates. Usually, the range between 5 % and 95 % of I_A is considered, and the corresponding time duration is denoted with $T_{5/95}$.

Fig. 3(a) shows the ground acceleration $\ddot{u}_g(t)$ recorded during the 1983 Trinidad offshore earthquake at the "Rio Dell Overpass, E Ground" station (horizontal component, azimuth angle = 0°), used in this section as an illustrative example. The Husid's function is reported in Fig. 3(b). A change in the slope of the function $J(t)$ denotes a change in the amplitude of the signal. The gray area shows the definition of the significant duration for this accelerogram. It is worth highlighting here that, although the earthquake record has a duration $T_g = 21.44$ s, the actual significant duration is $T_{5/95} = 7.715$ s.

6.1.2. Zero-level up-crossings

The frequency content of an accelerogram is directly related to the dynamic effects it can have on structural and geotechnical systems. While the Fourier analysis is a powerful tool to quantify the frequency content of the seismic signal, a preliminary insight can be provided by frequency of occurrence of zero-level up-crossings, i.e., crossings of the time axis with positive slope (e.g., [74–76]).

Fig. 3(c) plots the cumulative number of zero-level up crossings, $N_0^+(t)$, for the same illustrative accelerogram used in the previous sub-section. A change in the slope of the function $N_0^+(t)$ denotes a change in the frequency content of the accelerogram.

6.1.3. Significant frequency bandwidth

Considering the importance of time–frequency duality in the analysis of seismic signals, Fig. 4(a) shows the amplitude of the DFT (discrete Fourier transform) spectrum of the case-study accelerogram. Similar to the significant (time) duration defined above in conjunction with Husid's function, this sub-section introduces the new concept of "significant frequency bandwidth", $\Omega_{5/95}$. First, let $A_g(\omega)$ be the complex-valued Fourier transform of the accelerogram:

$$A_g(\omega) = \mathrm{FT}\left[\ddot{u}_g(t)\right] = \int_0^{T_g} \ddot{u}_g(t)\exp(-i\omega t)\mathrm{d}t\,, \tag{40}$$

in which $i = \sqrt{-1}$ is the imaginary unit. As a direct consequence of Parseval's theorem, one can prove that the Arias intensity can be calculated in the frequency domain as:

$$I_A = \frac{1}{2g}\int_0^{+\infty} |A_g(\omega)|^2 \mathrm{d}\omega; \tag{41}$$

hence, the cumulative distribution of the seismic signal in the frequency domain, normalised with respect to the Arias intensity (dual with respect to the Husid's function) can be defined as:

$$\widetilde{J}(\omega) = \frac{1/(2g)}{I_A}\int_0^{\omega} |A_g(s)|^2 ds\,, \tag{42}$$

with $0 \le \widetilde{J}(\omega) \le 1$.

The new function $\widetilde{J}(\omega)$ is illustrated in Fig. 4(b), where $\overline{\omega}_5$ and $\overline{\omega}_{95}$ are the circular frequencies corresponding to 5 % and 95 % of the Arias intensity, respectively; that is, $\widetilde{J}(\overline{\omega}_5) = 0.05$ and $\widetilde{J}(\overline{\omega}_{95}) = 0.95$. Thus, the significant frequency bandwidth (corresponding to the gray-shadowed area in Fig. 4(b)) can be defined as:

$$\Omega_{5/95} = \overline{\omega}_{95} - \overline{\omega}_5. \tag{43}$$

For the case-study accelerogram, $\overline{\omega}_5 = 10.26$ rad/s, $\overline{\omega}_{95} = 65.94$ rad/s, and $\Omega_{5/95} = 55.68$ rad/s.

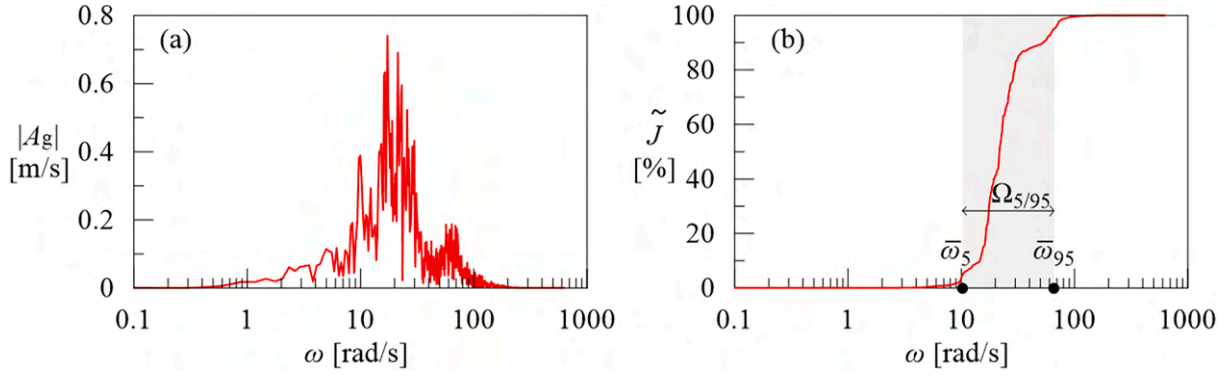

Fig. 4. Absolute value of the Fourier transform (FT) of the case-study accelerogram (a) and its cumulative energy distribution in the frequency domain, normalised to the Arias intensity (b).

6.2. Phase correlation

In this subsection, a novel correlation structure for defining the wavelets' random phases, to be applied in the generation of artificial accelerograms, is introduced.

The generic random phase $\phi_{j,k}$ can be considered as the discrete value of two-dimensional, mixed time–frequency-domain random field $Z(\omega, t)$, evaluated at the centre $P_{j,k} \equiv \{\overline{\omega}_j, \tau_{j,k}\}$ of the $\{j,k\}$th wavelet $\Psi_{j,k,\ell}$; that is $\phi_{j,k} \equiv Z\{\overline{\omega}_j, \tau_{j,k}\}$. Let now $\lambda_\tau = \Lambda_\tau T_{5/95}$ and $\lambda_\omega = \Lambda_\omega\ \Omega_{5/95}$ be the correlation lengths for this random field in the time domain and in the frequency domain, respectively, Λ_τ and Λ_ω being dimensionless measures of the correlation lengths normalised with respect to the significant duration $T_{5/95}$ and bandwidth $\Omega_{5/95}$ of the parent signal. Adopting an exponential auto-correlation function (ACF) for the generation of the random phases, one obtains:

$$\rho_{\phi\phi(j,k,J,K)} = \frac{\mathbb{E}\left[\phi_{j,k}\ \phi_{J,K}\right]}{\sigma_\phi^2} = \exp\left[-\sqrt{\left(\frac{\overline{\omega}_j - \overline{\omega}_J}{\Lambda_\omega\ \Omega_{5/95}}\right)^2 + \left(\frac{\tau_{j,k} - \tau_{J,K}}{\Lambda_\tau\ T_{5/95}}\right)^2} \right], \tag{44}$$

in which the square root in the right-hand side of Eq. (44) is a scaled distance between the two wavelet centres $P_{j,k}$ and $P_{J,K}$. The limiting condition $\Lambda_\omega \to 0$ and $\Lambda_\tau \to 0$ corresponds to the case where all the random phases are uncorrelated (UC), i.e., where $\rho_{\phi\phi(j,k,J,K)} = \delta_{j,J}\ \delta_{k,K}$, such that $\rho_{\phi\phi(j,k,J,K)} = 0$ if $\{j, k\} \neq \{J, K\}$.

Conversely, the case of fully correlated (FC) phases occurs when simultaneously $\Lambda_\omega \to +\infty$ and $\Lambda_\tau \to +\infty$, i.e., where $\rho_{\phi\phi(j,k,J,K)} = 1$ for any pairs $\{j,k\}$ and $\{J, K\}$. Other interesting cases occur when only one of the correlation measures Λ_τ and Λ_ω goes to infinity. When $\Lambda_\tau \to +\infty$, Eq. (44) simplifies as:

$$\rho_{\phi\phi(j,k,J,K)} = \exp\left(-\frac{\left|\overline{\omega}_j - \overline{\omega}_J\right|}{\Lambda_\omega\ \Omega_{5/95}} \right); \tag{45}$$

accordingly, all the random phases in the same bandwidth j, with $j = 1, 2, \cdots, M$, become fully correlated; that is, $\phi_{j,0} \equiv \phi_{j,1} \equiv \ldots \equiv \phi_{j,b_j-1}$, meaning that the whole contribution of the jth bandwidth to the reconstruction of the parent signal will be phase-shifted of the same random angle $\phi_{j,0}^{(r)}$ when generating the rth sample $F_\ell^{(r)}$. Similarly, when $\Lambda_\omega \to +\infty$, Eq. (44) simplifies as:

$$\rho_{\phi\phi(j,k,J,K)} = \exp\left(-\frac{\left|\tau_{j,k} - \tau_{J,K}\right|}{\Lambda_\tau\ T_{5/95}} \right); \tag{46}$$

in this case, irrespectively of the frequency bands they belong to, the closer the time instants $\tau_{j,k}$ and $\tau_{J,K}$ at which the wavelets $\Psi_{j,k,\ell}$ and $\Psi_{J,K,\ell}$ are centered, the stronger the correlation between the corresponding random phases $\phi_{j,k}$ and $\phi_{J,K}$.

6.3. Application of the randomization procedure to recorded accelerograms

In this subsection, the wavelet-based method has been applied to three recorded accelerograms with entirely distinct time and frequency characteristics, to highlight the remarkable versatility and adaptability of the proposed procedure to deal with any seismic input. Since the results of the proposed wavelet-based method depend on a dual choice, i.e., the subdivision of the frequency domain into a certain number of M frequency bands and the type of the correlation structure adopted for the random phases, both aspects are investigated for each of the three analyzed signals. The main time and frequency properties of the selected accelerograms (Trinidad offshore 1983, Imperial Valley-06 1979 and Landers 1992), are listed in Table 1: time duration t_{2N}, sampling step Δt, sampling frequency ν_0, number of discrete non-zero frequencies N, Nyquist frequency ω_N, and frequency step $\Delta\omega$.

Different sets composed by $N_s = 1000$ child signals have been generated by using Eq.(15) and baseline corrected (e.g. [77–80]) with a best-fit polynomial curve of order ≥ 2. This polynomial is determined for each child sample through a least-squares regression analysis and is then subtracted from the acceleration time history, so that the end ground velocity is zero and any physically inconsistent trends in the slowly varying moving average of the ground displacement time history are removed.

6.3.1. Trinidad offshore earthquake

The first horizontal component of the 1983 Trinidad offshore earthquake, depicted in Fig. 3a, has been used in the following as parent accelerogram. The selected ground motion, downloaded from PEER [2] database and characterised by moment magnitude $M_w = 5.7$ and Joyner-Boore site-to-source distance R_{JB}=68.02 km, has been recorded by a station having an average shear wave velocity in the upper 30 m equal to $V_{s,30} = 311.75$ m/s. The selected motion of time duration t_{2N}=21.44 s, sampling step $\Delta t = 0.005$ s and peak

Table 1
Main time and frequency properties of the selected accelerograms.

Earthquake	t_{2N} [s]	Δt [s]	ν_0 [Hz]	N	ω_N [rad/s]	$\Delta\omega$ [rad/s]
Trinidad offshore	21.44	0.005	200	2144	628.319	0.293
Imperial Valley	37.86	0.005	200	3786	628.319	0.166
Landers	48.12	0.005	200	4812	628.319	0.13

ground acceleration PGA=1.72 m/s^2, is characterized by an Arias intensity equal to I_A=0.17 m/s. The mean period, determined to characterize the frequency content of the parent signal, has been evaluated according to Rathie et al. [81] and is equal to $T_m = 0.32$ s, corresponding to a mean circular frequency $F_m = 2\pi/ T_m = 20.03$ rad/s.

Aimed at investigating different options for the circular wavelet-based randomisation of the parent record, the effect of alternative subdivisions of the frequency range [0, ω_N=628.32 rad/s] into:

- M=1, and M=N intervals of equal-spaced-bandwidths (ESB), have been studied to highlighted how the trade-off between localizations in time and frequency domains plays a fundamental role for the generation of meaningful time histories of ground acceleration. For M=1 there is only a single frequency band with a bandwidth $B_1 = 628.32$ rad/s, being $b_1 = 2144$; while for M=N=2144, each frequency band consists of a single discrete frequency ($b_1 = b_2$=…=b_N=1) and all the N bandwidths have the same amplitude $B_1 = B_2$=…=B_N=0.293 rad/s;
- M=10 intervals of constant-intensity-bandwidths (CIB), evaluated as the frequencies corresponding to the value released by cumulative distribution of the seismic signal in the frequency domain, normalised with respect to the Arias intensity, $\widetilde{J}(\omega)$. The representation of the subdivision of the function $\widetilde{J}(\omega)$ considering M=10 bands, is reported in Fig. 5. The main parameters of each j frequency band belonging to the partition of the parent signal into M=10 constant-intensity-bandwidths, have been listed in Table 2.

Furthermore, in order to investigate the effect of the exponential auto-correlation function (ACF) for the generation of the random phases (see Eq.(44)), three different correlation structures have been adopted for each of the three M partitions of the frequency domain. Specifically:

- for the two extreme cases with M=1 and M=N intervals of equal-spaced-bandwidths (ESB), have been considered the following correlation measures:
  i) $\Lambda_\omega = \Lambda_\tau \to 0$ (UC case);
  ii) $\Lambda_\omega = \Lambda_\tau = 1$ (PC case);
  iii) $\Lambda_\omega = \Lambda_\tau \to \infty$ (FC case);
- for the intermediate case with M=10 constant-intensity-bandwidths (CIB), have been analysed the results that occur when both the dimensionless measures of the correlation lengths are unitary and when only one of the correlation measures goes to infinity:

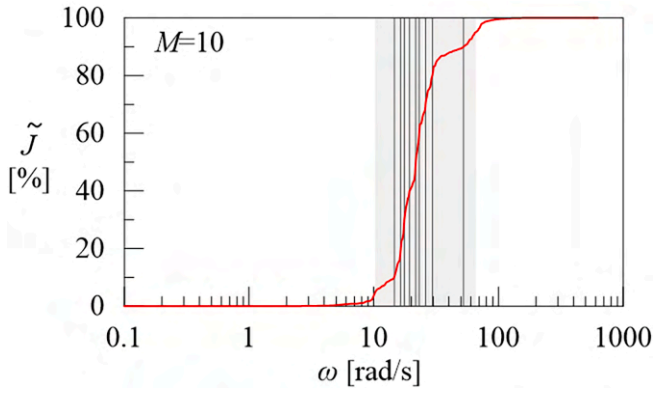

Fig. 5. Normalised cumulative energy distribution in the frequency domain of the parent signal (red line) together with the frequency band subdivision assuming M=10 (vertical lines) and with significant frequency bandwidth (grey area).

Table 2
Main characteristics of each frequency band belonging to jth partition in M=10 bands: Trinidad offshore earthquake.

$\widetilde{J}(\omega)$ [%]	j	m_j	n_j	b_j	ω_{m_j} [rad/s]	ω_{n_j} [rad/s]	B_j [rad/s]
0–10	1	0	50	50	0	14.65	14.65
10–20	2	50	56	6	14.65	16.41	1.76
20–30	3	56	60	4	16.41	17.58	1.17
30–40	4	60	66	6	17.58	19.34	1.76
40–50	5	66	74	8	19.34	21.68	2.34
50–60	6	74	79	5	21.69	23.15	1.47
60–70	7	79	89	10	23.15	26.08	2.93
70–80	8	89	101	12	26.08	29.60	3.52
80–90	9	101	179	78	29.60	52.46	22.86
90–100	10	179	2144	1965	52.46	628.32	575.86

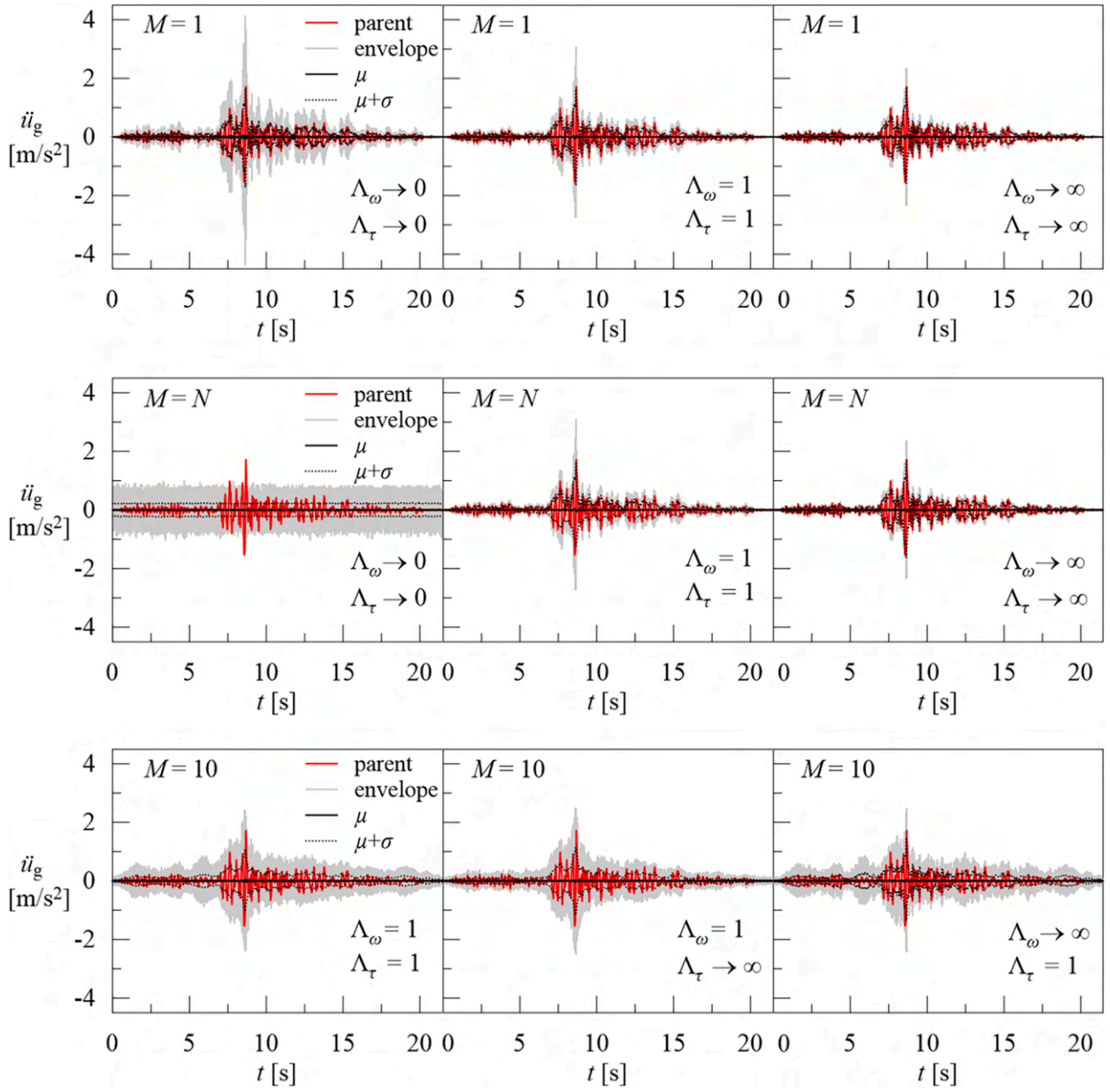

Fig. 6. Parent accelerogram together with the statistics of the generated child signals, considering a subdivision of the frequency domain in M=1 and M=N=2144 equal-spaced frequencies bands and for M=10 constant-intensity-bandwidths, assuming three different values of the correlation measures Λ_ω and Λ_τ: Trinidad offshore earthquake.

i) $\Lambda_\omega = \Lambda_\tau = 1$ (PC case);
ii) $\Lambda_\omega = 1$ and $\Lambda_\tau \to \infty$ (PC case);
iii) $\Lambda_\omega \to \infty$ and $\Lambda_\tau = 1$ (PC case).

Finally, nine sets composed by $N_s = 1000$ child signals have been generated by using Eq. (15).

In Fig. 6 are reported the parent signal (red line) together with the corresponding statistics of the N_s generated child signals namely: *i*) mean value μ (solid black line); *ii*) bounds of the confidence interval corresponding to mean plus/minus one standard deviation σ (black dotted lines), *iii*) maximum-minimum envelope of the generated signals (shadowed grey area), for the nine analysed cases.

From the analysis of the bounds of the confidence interval, it can be noticed that for M=1 the variation in amplitude of the generated child signals appear to be preserved for all the three adopted correlations structures while for M=N=2144, the temporal evolution of the amplitude of the generated child signals appears to be preserved only for the PC ($\Lambda_\omega = \Lambda_\tau = 1$) and FC ($\Lambda_\omega = \Lambda_\tau \to \infty$) cases. In fact, when M=N and $\Lambda_\omega = \Lambda_\tau \to 0$ (UC case), the generated child signals tend to lose the fidelity in terms of non-stationary

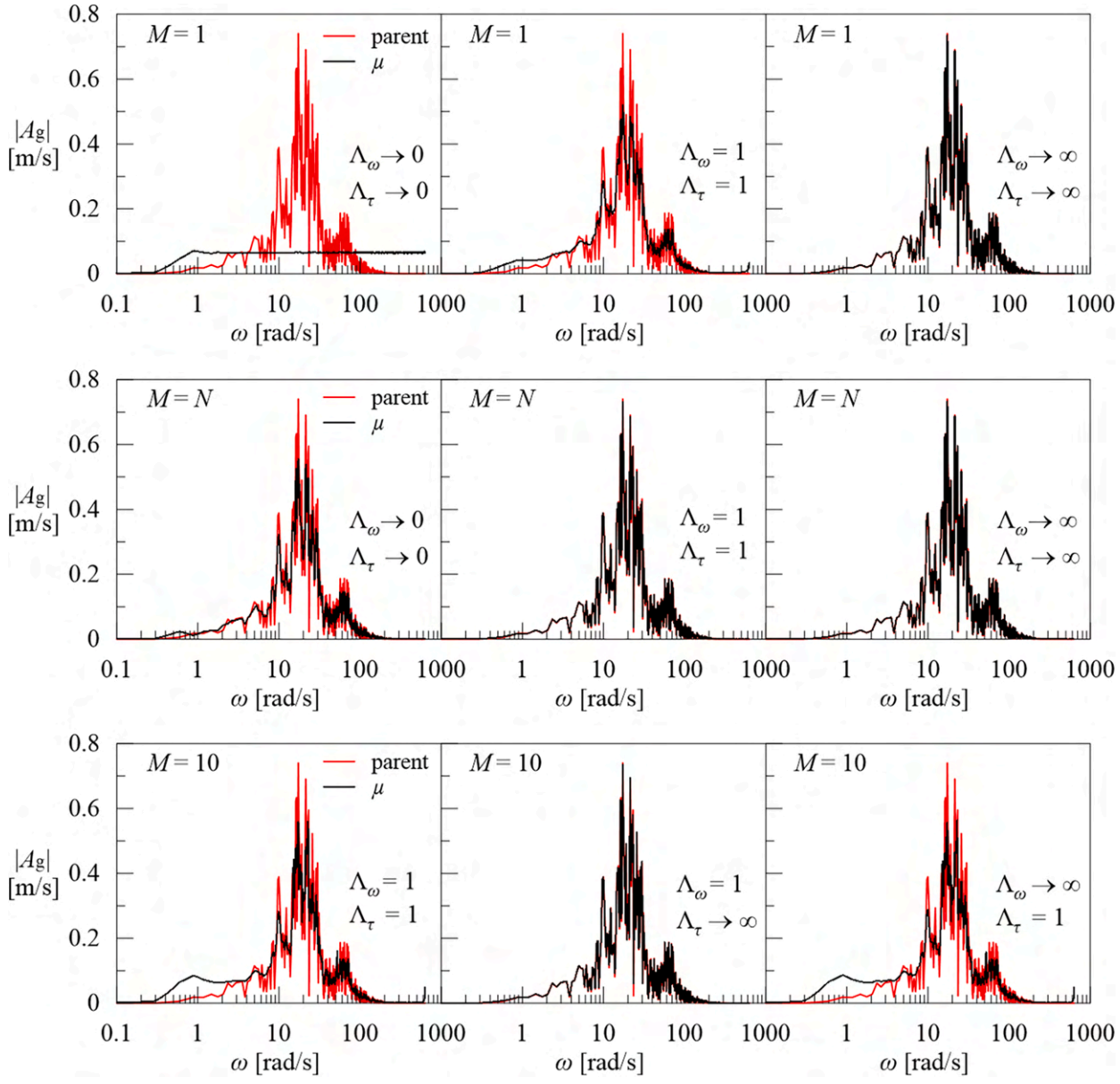

Fig. 7. Comparison between Fourier spectrum modulus of the parent signal and the mean spectrum of the generated signals, considering a subdivision of the frequency domain in M=1 and M=N=2144 equal-spaced frequencies bands and for M=10 constant-intensity-bandwidths, assuming three different values of the correlation measures Λ_ω and Λ_τ: Trinidad offshore earthquake.

characteristics, and they become realizations of a stationary process with no information preserved in the time domain.

The opposite situation occurs in the frequency domain in fact, for the UC case, as the number of bands increases, the fidelity in representing the frequency content also increases. This effect is highlighted in Fig. 7 in which the mean values of the modules of the Fourier spectra are compared with the target one. In fact, the case in which M=1 (i.e. there is only a single frequency band) and $\Lambda_\omega = \Lambda_\tau \to 0$ (UC case), leads to a random process in which information about the distribution of energy is lost in the frequency domain. This extreme case doesn't preserve the frequency characteristics of the original seismic record, in fact the mean amplitude Fourier spectrum is nearly flat.

The adoption of the correlation structure with $\Lambda_\omega = \Lambda_\tau = 1$ enhances the fidelity of the generated samples to match the frequency content of the target signal. For M=10, the fidelity in mimicking both the variation in time and the frequency content of the parent signal appears to be preserved for all the three adopted correlation measures.

A further comparison is presented in terms of Husid's function J, cumulative zero-level up-crossing functions $N_0^+(t)$, and elastic response spectra $S_a(T_0, \zeta_0)$ (computed assuming the equivalent viscous damping ratio $\zeta_0 = 0.05$), which are shown in Figs. 8-10 along

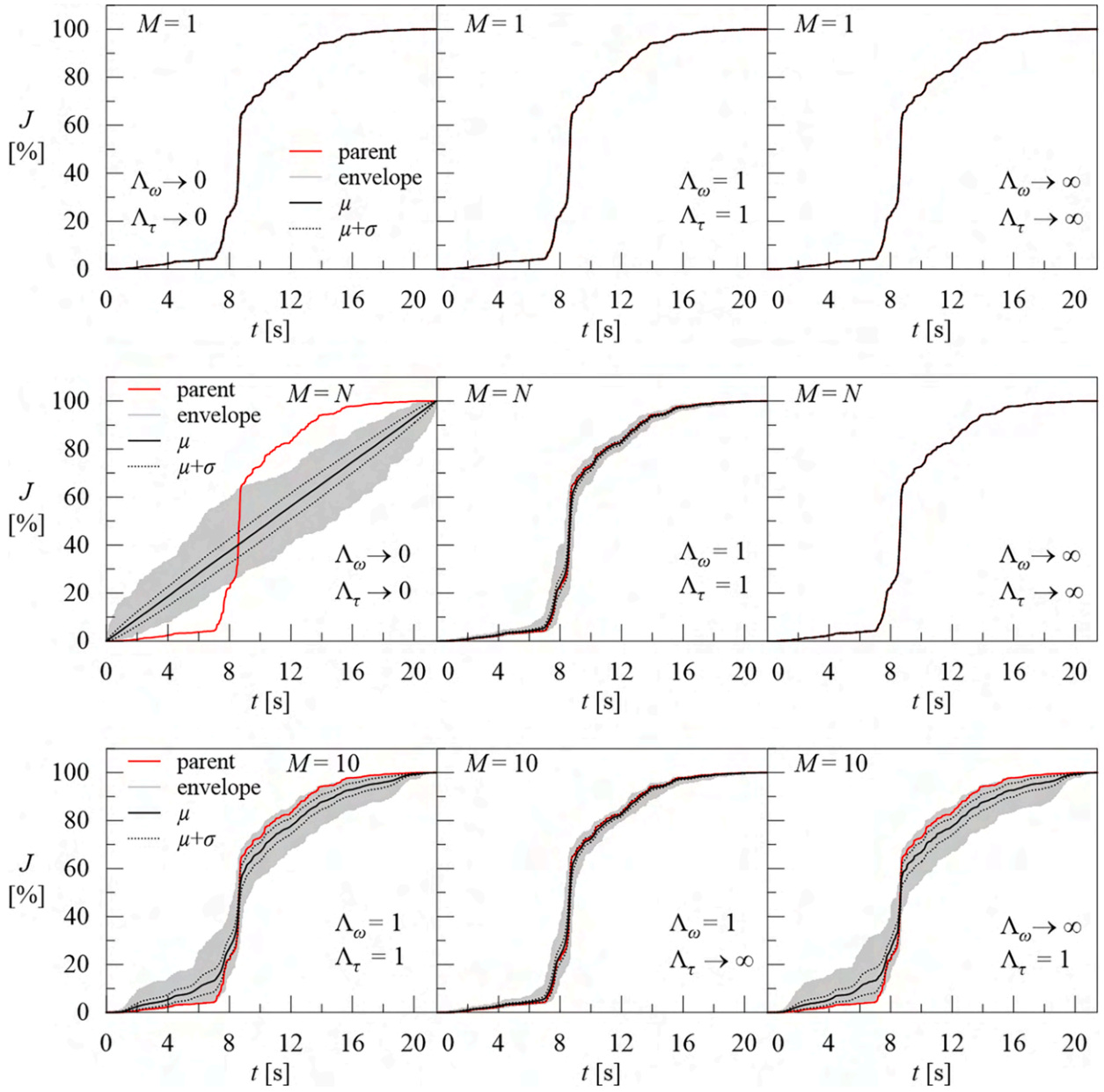

Fig. 8. Percentage Husid's function of the parent signal (red lines) together with the mean one of the generated child signals (black solid lines); the mean ± one standard deviation (black dotted lines); the maximum and the minimum values for whole set of generated signals (grey shaded area), considering a subdivision of the frequency domain in M=1 and M=N=2144 equal-spaced frequencies bands and for M=10 constant-intensity-bandwidths, assuming three different values of the correlation measures Λ_ω and Λ_τ: Trinidad offshore earthquake.

with the corresponding statistics.

Fig. 8 shows that the mean percentage Husid's function J of the generated child signals is in a good agreement with the parent one in all the analysed configurations except for the UC case in correspondence of a subdivision of the frequency range into M=N=2144 parts. In this case, the linear trend of the percentage Husid's function is caused by the fact that the child signals are samples of a stationary process.

From the analysis of the shadowed grey area it can be noticed that for M=10, the percentage Husid's functions J of the samples belonging to sets evaluated with $\Lambda_\omega = \Lambda_\tau = 1$ and $\Lambda_\omega \to \infty$, $\Lambda_\tau = 1$ assume a great variability. This means that the adoption of the auto-correlation function for the generation of random phases allows to obtain signals having characteristics totally different from each other although they have the same average function.

Fig. 9 shows that the mean cumulative zero-level up crossing functions of the child signals are very close to the target one in all the analysed situations except for the uncorrelated case (UC) with M=1. In this case (M=1 and $\Lambda_\omega = \Lambda_\tau \to 0$), the only frequency band

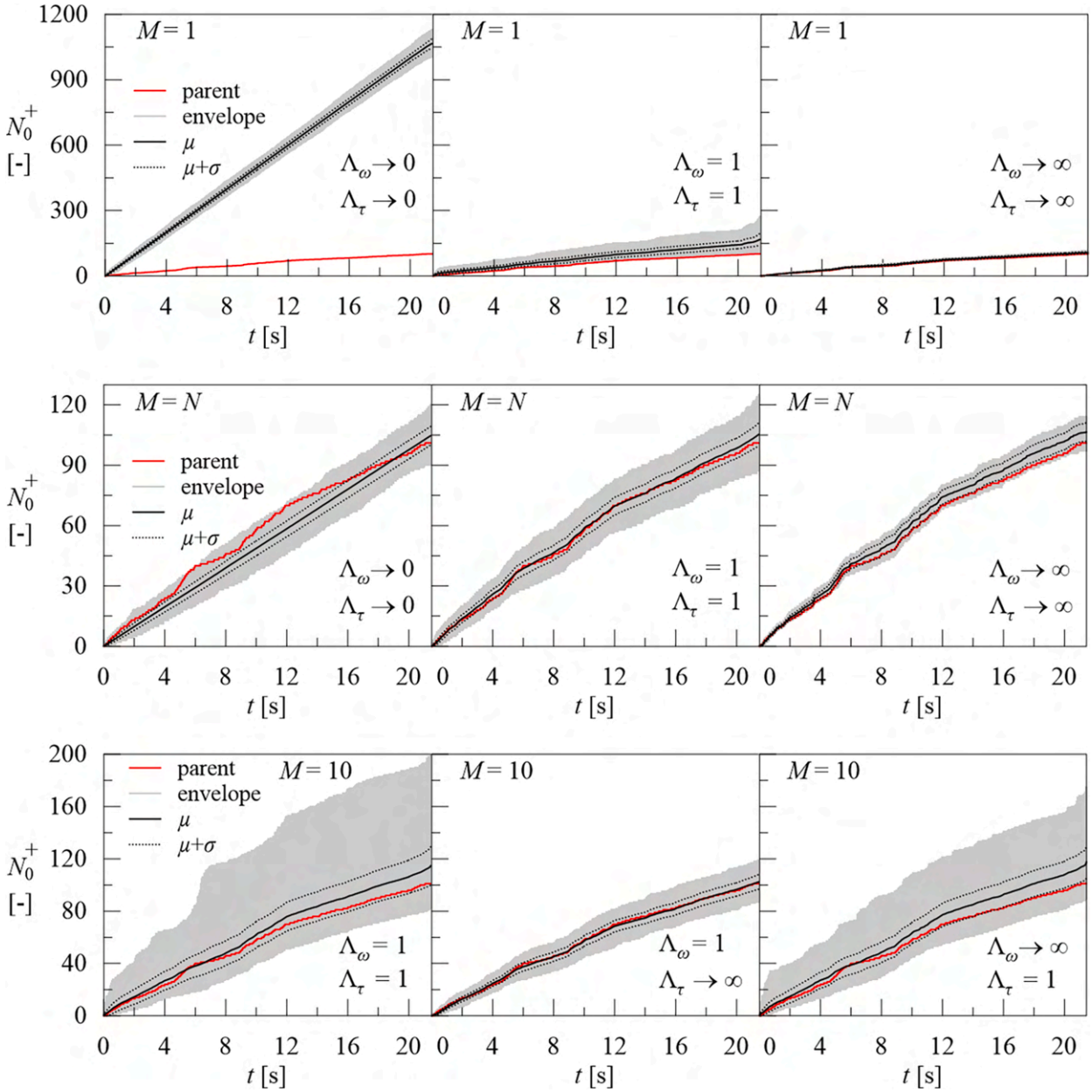

Fig. 9. Cumulative zero level up crossing function of the parent signal together with the statistics of the generated signals, considering a subdivision of the frequency domain in M=1 and M=N=2144 equal-spaced frequencies bands and for M=10 constant-intensity-bandwidths, assuming three different values of the correlation measures Λ_ω and Λ_τ: Trinidad offshore earthquake.

makes the generated signals as uniformly modulated samples of a white noise having a far larger number of high-frequency fluctuations. As a result, the zero-level up-crossing function (black line) heavily overestimates the parent signal (red line).

For the UC case of the M=1 and M=N frequency partitions, the mean acceleration response spectra of the generated child signals (black solid lines), shown in Fig. 10 versus the oscillator's undamped natural period of vibration T_0, are very far to that of the target one (red line). In all the other investigated configurations the mean acceleration response spectra are in a good agreement with the trend of the parent one.

In this subsection, the extreme cases of M=1 and M=N have been presented for illustrative purposes considering all three correlation structures discussed in the paper. However, given that in the FC case, regardless of the subdivision of the frequency domain, all the realizations of the random phases coincide to each other, this correlation structure is not adequate to obtain the desired variability

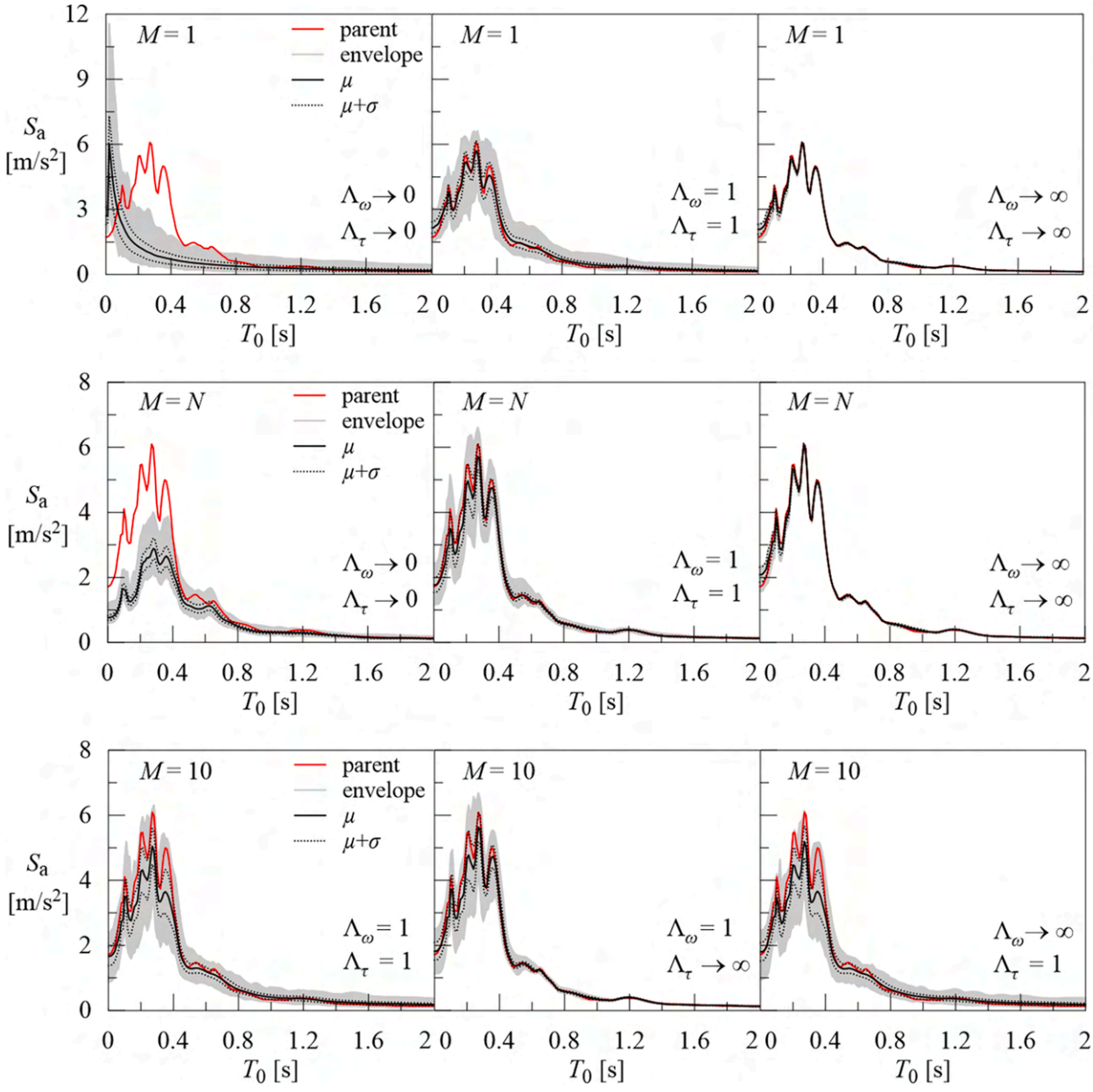

Fig. 10. Acceleration response spectrum of the parent signal together with the mean one of the generated child signals; the mean ± one standard deviation; the maximum and the minimum values for whole set of generated signals, considering a subdivision of the frequency domain in M=1 and M=N=2144 equal-spaced frequencies bands and for M=10 constant-intensity-bandwidths, assuming three different values of the correlation measures Λ_ω and Λ_τ: Trinidad offshore earthquake.

of the samples. In fact, all child signals closely resemble the parent one. The analysis of the extreme cases, M=1 and M=N, revealed that the introduction of a correlation structure results in generated samples that closely match the characteristics of the parent signal. Therefore, it is recommended to use the PC structure for achieving the best results. Thus, the purpose of examining the intermediate case M=10 is to understand the outcomes achieved by generating samples exclusively with the suggested correlation structure.

To ensure a comprehensive understanding of the results, analyses have also been conducted for the two specific cases of the correlation structure described in Section 6.2, i.e., when only one of the two correlation measures goes to infinity (see Eqs.(45) and (46)).

Table 3
Main characteristics of each frequency band belonging to jth partition in M=5 bands: Imperial Valley earthquake.

$\widetilde{J}(\omega)$ [%]	j	m_j	n_j	b_j	ω_{m_j} [rad/s]	ω_{n_j} [rad/s]	B_j [rad/s]
0–20	1	0	36	36	0	5.97	5.97
20–40	2	36	79	43	5.97	13.11	7.14
40–60	3	79	116	37	13.11	19.25	6.14
60–80	4	116	164	48	19.25	27.22	7.97
80–100	5	164	3786	3622	27.22	628.32	601.10

Table 4
Main characteristics of each frequency band belonging to jth partition in M=10 bands: Imperial Valley earthquake.

$\widetilde{J}(\omega)$ [%]	j	m_j	n_j	b_j	ω_{m_j} [rad/s]	ω_{n_j} [rad/s]	B_j [rad/s]
0–10	1	0	12	12	0	1.99	1.99
10–20	2	12	36	24	1.99	5.97	3.98
20–30	3	36	61	25	5.97	10.12	4.15
30–40	4	61	79	18	10.12	13.11	2.99
40–50	5	79	103	24	13.11	17.09	3.98
50–60	6	103	116	13	17.09	19.25	2.16
60–70	7	116	121	5	19.25	20.08	0.83
70–80	8	121	164	43	20.08	27.22	7.14
80–90	9	164	254	90	27.22	42.15	14.94
90–100	10	254	3786	3532	42.15	628.32	586.17

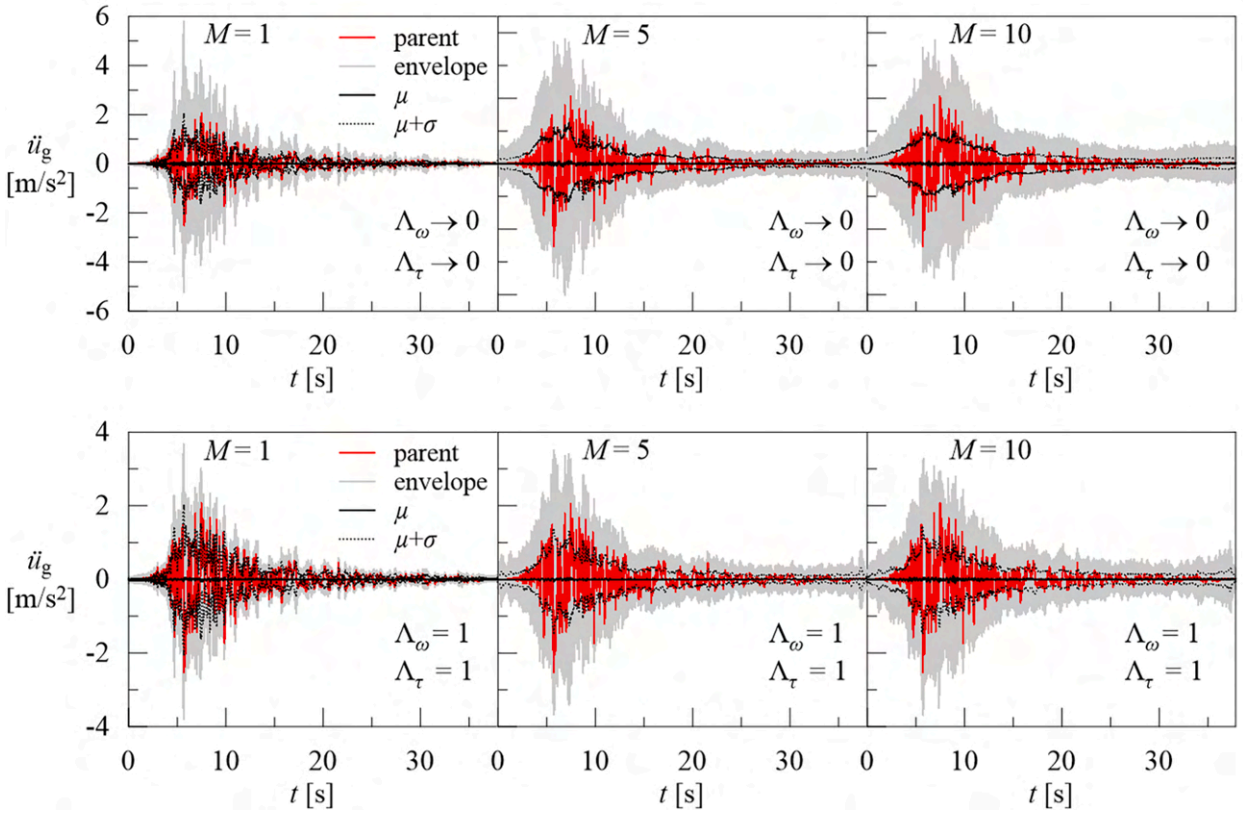

Fig. 11. Parent accelerogram together with the statistics of the generated child signals, considering a subdivision of the frequency domain in M=1,5,10 constant-intensity-bandwidths assuming two different correlation structures Λ_ω and Λ_τ: Imperial Valley earthquake.

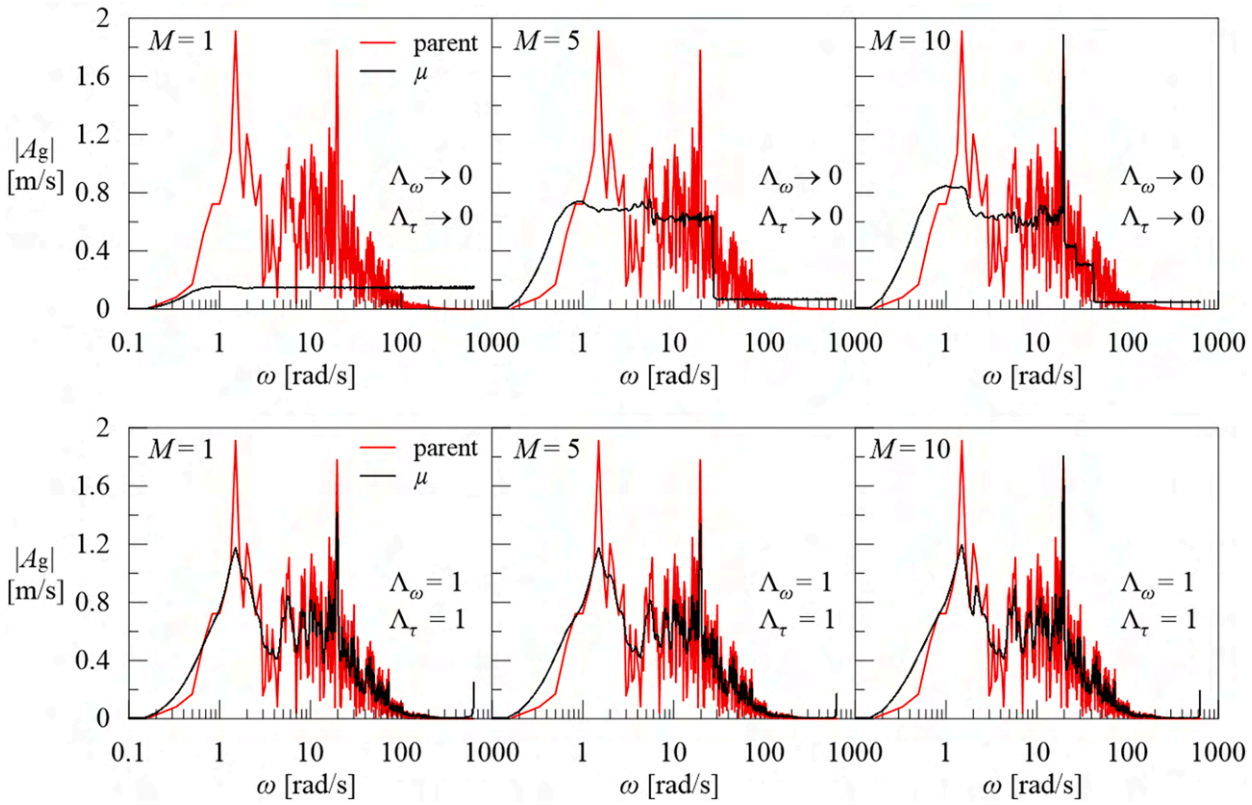

Fig. 12. Comparison between Fourier spectrum modulus of the parent signal and the mean spectrum of the generated ones, considering a subdivision of the frequency domain in M=1,5,10 constant-intensity-bandwidths, assuming two different correlation structures Λ_ω and Λ_τ: Imperial Valley earthquake.

6.3.2. *Imperial Valley earthquake*

In this subsection the first horizontal component (HVP225) of the 1979 Imperial Valley-06 accelerogram that is a typical pulse-like velocity ground motion with a pulse period of $T_p = 4.8$ s [8], has been assumed as parent signal. The selected motion of magnitude $M_w = 6.53$, site-to-source distance R_{JB}=5.35 km, overall duration t_{2N}=37.86 s and peak ground acceleration PGA=2.53 m/s^2, is characterized by an Arias intensity equal to I_A=0.885 m/s. The recording station, located at the Holtville Post Office, sits on deep deposits of dense sand with a shear wave velocity $V_{s,30} = 202.89$ m/s. The mean period of the parent signal is equal to $T_m = 0.93$ s, corresponding to a mean circular frequency equal to $F_m = 6.79$ rad/s. The significant duration and frequency bandwidth are equal to $T_{5/95} = 11.81$ s and $\Omega_{5/95} = 50.45$ rad/s, respectively.

As highlighted by the results obtained from the application of the proposed method to the test signal (Section 5) and to a recorded seismic accelerogram (Section 6.3.1), the case of fully correlated (FC) random phases represents a limiting model that minimizes the variability of generated random samples. Therefore, only the effect of uncorrelated (UC) and partially correlated (PC) random phases will be investigated in the following by using the correlation function introduced in Eq.(44). Specifically, when $\Lambda_\omega \to 0$ and $\Lambda_\tau \to 0$ all random phases are uncorrelated (UC), while the condition $\Lambda_\omega = 1$ and $\Lambda_\tau = 1$ implies that to all random phases being partially correlated (PC).

The effect of alternative subdivisions of the frequency range [0, ω_N=628.32 rad/s] into M=1, M=5 and M=10 constant-intensity-bandwidths (CIB), evaluated as the frequencies corresponding to the value released by the normalised cumulative distribution of the seismic signal in the frequency domain, $\widetilde{J}(\omega)$, have been investigated. For M=1 there is only a single frequency band with a bandwidth $B_1 = 628.32$ rad/s, being $b_1 = 3786$. The main parameters of each j frequency band belonging to the partition of the parent signal into M=5 and M=10 constant-intensity-bandwidths, have been listed in Table 3 and 4, respectively.

In Fig. 11 are reported the parent signal (red line) together with the corresponding statistics of the $N_s = 1000$ child signals, generated by using Eq.(15). From the analysis of the bounds of the confidence intervals, it can be noticed that the variation in amplitude of the generated signals appear to be preserved for all the three subdivision of the frequency domain (M=1,5,10) and for

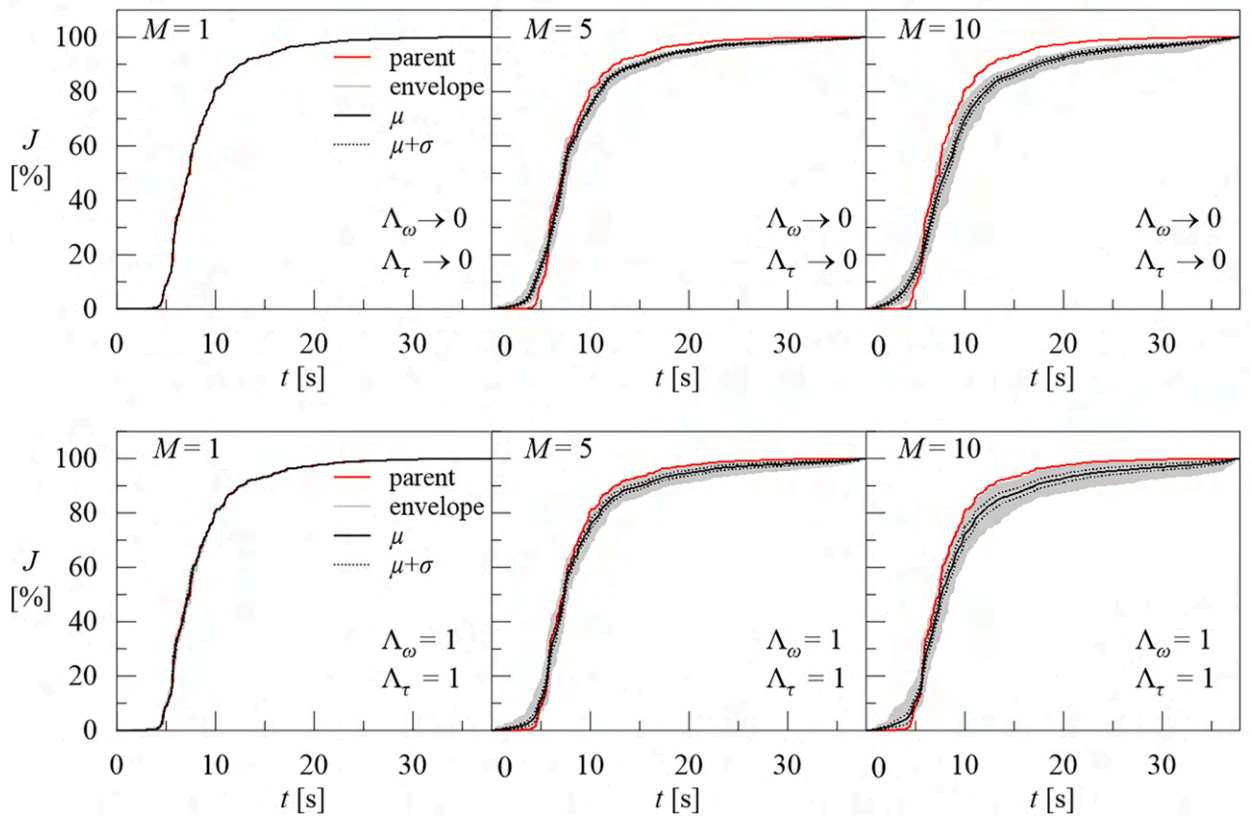

Fig. 13. Percentage Husid's function of the parent signal together with the statistics of the generated signals, considering a subdivision in M=1,5,10 constant-intensity-bandwidths, assuming two different values of the correlation measures Λ_ω and Λ_τ: Imperial Valley earthquake.

both the adopted correlations structures (UC and PC).

In Fig. 12 the mean values of the modules of the Fourier spectra of the generated signals are compared with the parent one. The adoption of the correlation structure of Eq. (44) with $\Lambda_\omega = \Lambda_\tau = 1$ ensures that for all frequency domain partitions, there is always an excellent match between the mean amplitude Fourier spectrum of the generated signals and the target one.

In the case of uncorrelated phases ($\Lambda_\omega = \Lambda_\tau \to 0$), for the three subdivision of the frequency domain, the mean amplitude Fourier spectra do not exhibit a similar trend to the target spectrum. When M=1, the mean spectrum appears as a constant function, so in the generated samples there is a total loss of information regarding the original frequency content of the parent signal.

A further comparison is represented in terms of percentage Husid's function J and cumulative zero-level up crossing functions $N_0^+(t)$, that are reported in Figs. 13 and 14 together with the corresponding statistics.

It can be observed that the assumption of partially correlated random phases ensures that the characteristics of the parent signal are always in a good agreement with the functions computed for the generated samples. Furthermore, the variability of the functions of the child samples increases as the number of considered bands increases too.

6.3.3. Landers earthquake

In this subsection the second horizontal component of the 1992 Landers ground motion (LCN345), has been assumed as parent signal. The selected accelerograms of magnitude $M_w = 7.28$, site-to-source distance R_{JB}=2.19 km, overall duration t_{2N}=48.12 s and peak ground acceleration PGA=6.19 m/s^2, is characterized by an Arias intensity equal to I_A=6.58 m/s. The recording station, located at Lucerne, sits on rock deposits with a shear wave velocity $V_{s,30} = 1369.0$ m/s. The mean period of the parent signal is equal to $T_m = 0.15$ s, corresponding to a mean circular frequency equal to $F_m = 39.99$ rad/s. The significant duration and frequency bandwidth are equal to $T_{5/95} = 13.78$ s and $\Omega_{5/95} = 160.61$ rad/s, respectively.

The effect of subdivision of the frequency range [0, ω_N=628.32 rad/s] into M=1, M=5 and M=10 constant-intensity-bandwidths (CIB) and the influence of the uncorrelated (UC: $\Lambda_\omega \to 0$ and $\Lambda_\tau \to 0$) and partially correlated (PC: $\Lambda_\omega = 1$ and $\Lambda_\tau = 1$) random phases in

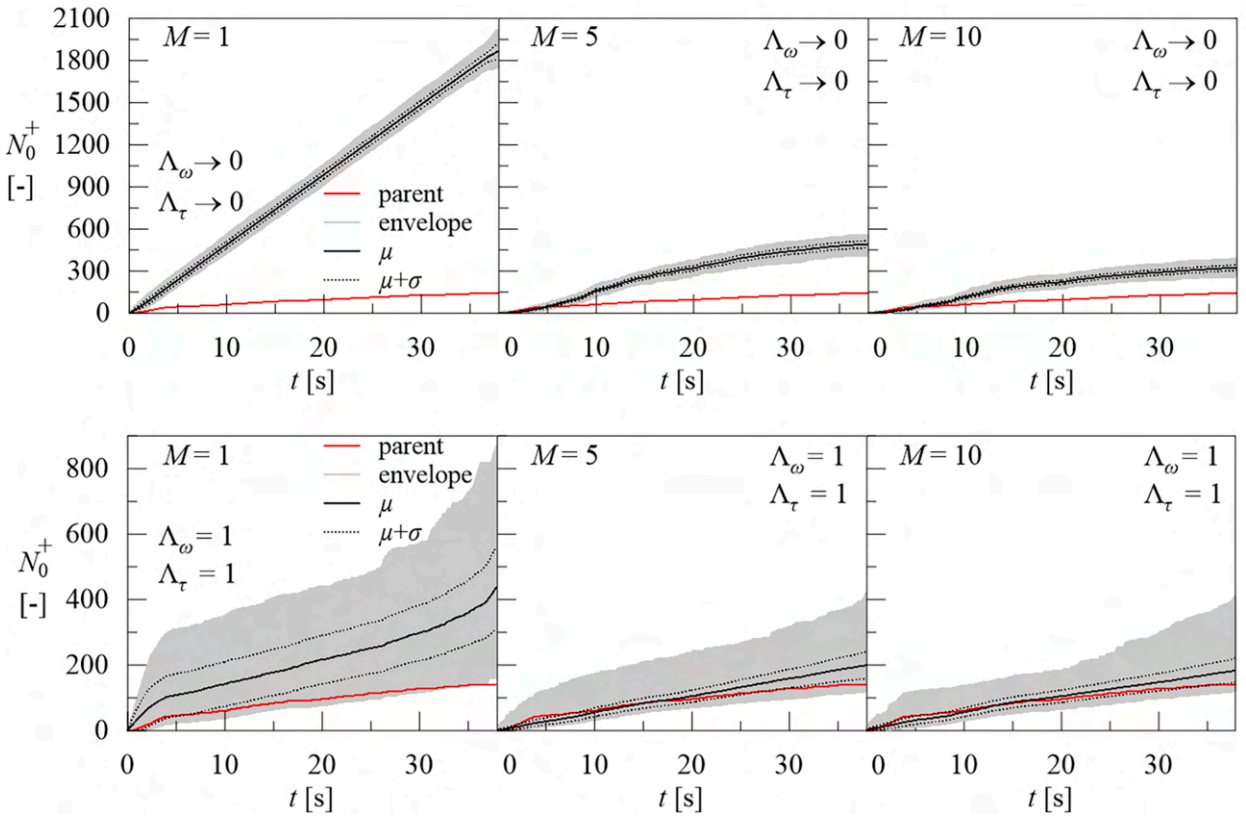

Fig. 14. Cumulative zero level up crossing function of the parent signal together with the statistics of the generated signals, considering a sub-division in M=1,5,10 constant-intensity-bandwidths, for two different correlation measures Λ_ω and Λ_τ: Imperial Valley earthquake.

Table 5
Main characteristics of each frequency band belonging to jth partition in M=5 bands: Landers earthquake.

$\widetilde{J}(\omega)$ [%]	j	m_j	n_j	b_j	ω_{m_j} [rad/s]	ω_{n_j} [rad/s]	B_j [rad/s]
0–20	1	0	295	295	0	38.52	38.52
20–40	2	295	452	157	38.52	59.02	20.50
40–60	3	452	565	113	59.02	73.77	14.75
60–80	4	565	809	244	73.77	105.63	31.86
80–100	5	809	4812	4003	105.63	628.32	522.69

Table 6
Main characteristics of each frequency band belonging to jth partition in M=10 bands: Landers earthquake.

$\widetilde{J}(\omega)$ [%]	j	m_j	n_j	b_j	ω_{m_j} [rad/s]	ω_{n_j} [rad/s]	B_j [rad/s]
0–10	1	0	194	194	0	25.33	25.33
10–20	2	194	295	101	25.33	38.52	13.19
20–30	3	295	351	56	38.52	45.83	7.31
30–40	4	351	452	101	45.83	59.02	13.19
40–50	5	452	521	69	59.02	68.03	9.01
50–60	6	521	565	44	68.03	73.77	5.75
60–70	7	565	639	74	73.78	83.44	9.66
70–80	8	639	809	170	83.44	105.63	22.20
80–90	9	809	1058	249	105.63	138.15	32.51
90–100	10	1058	4812	3754	138.15	628.32	490.17

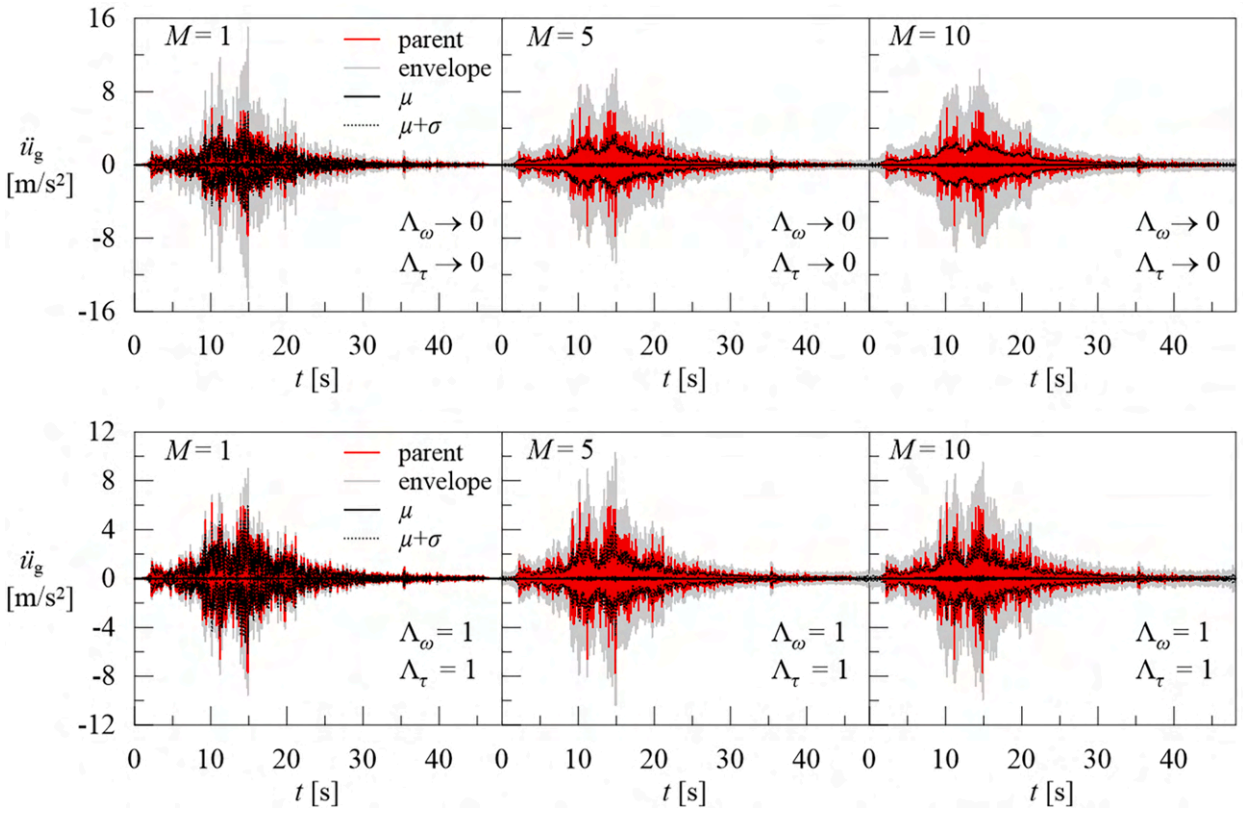

Fig. 15. Parent accelerogram together with the statistics of the generated child signals, considering a subdivision of the frequency domain in M=1,5,10 constant-intensity-bandwidths assuming two different correlation structures Λ_ω and Λ_τ: Landers earthquake.

the generation procedure, are investigated. For M=1 there is only a single frequency band with a bandwidth $B_1 = 628.32$ rad/s, being $b_1 = 4812$. The main parameters of each j frequency band belonging to the partition of the parent signal into M=5 and M=10 constant-intensity-bandwidths, have been listed in Table 5 and 6, respectively. In Fig. 15, the parent signal is depicted (red line), alongside the statistical data for 1000 child signals generated using Eq. (15). An examination of the confidence intervals reveals that amplitude variations in the generated signals remain consistent across all three frequency domain subdivisions (M=1, 5, 10) and under both adopted correlation structures. Fig. 16 compares the mean values of the Fourier spectra modules of the generated signals with the parent one. The use of the correlation structure outlined in Eq. (49) with $\Lambda_\omega = \Lambda_\tau = 1$ ensures that, across all frequency domain partitions, there is a consistent and excellent match between the mean amplitude Fourier spectrum of the generated signals and the target spectrum. In cases of uncorrelated phases ($\Lambda_\omega = \Lambda_\tau \to 0$), the mean amplitude Fourier spectra do not exhibit a similar trend to the target one. Especially when M=1, the mean spectrum appears nearly flat, resulting in a complete loss of information about the original frequency content of the parent signal. A further comparison is presented concerning the percentage Husid's function J and cumulative zero-level up crossing function $N_0^+(t)$, as reported in Figs. 17 and 18, along with their respective statistics. It is evident that the assumption of partially correlated random phases ensures that the characteristics of the parent signal consistently align well with the functions computed for the generated samples. Moreover, the variability of these functions in the child samples increases as the number of considered bands also increases.

6.4. Discussion

The numerical results have shown that the choice of the number and size of bands used to partition the frequency domain of the parent accelerogram greatly influences the accuracy of the analysis. The subdivision of the frequency domain of the selected signal depends on key factors, including the analysis objectives, available computational resources, signal characteristics, and the desired level of precision. A denser number of bands should be used when the main goal is to analyse and capture very detailed frequency variations within the signal as it develops over time. Using a reduced number of bands provides a more general and less detailed view

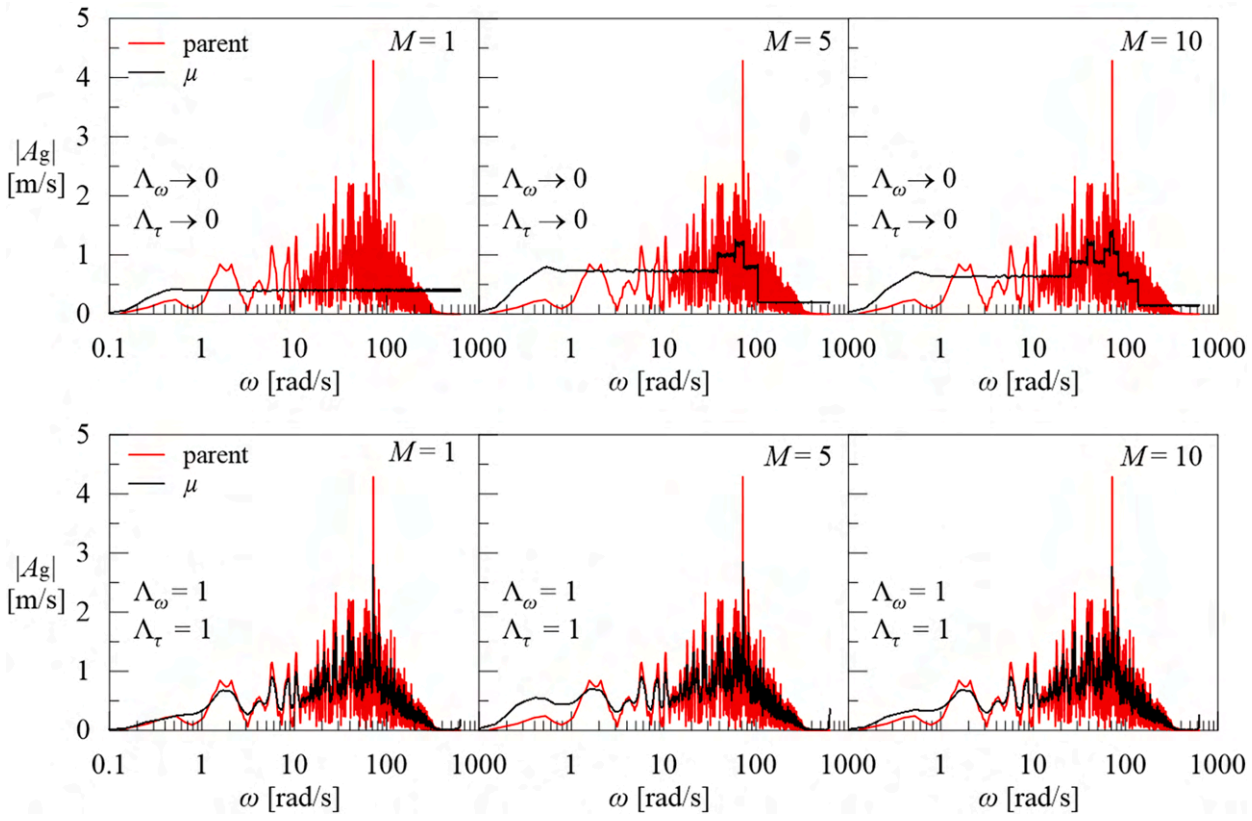

Fig. 16. Comparison between Fourier spectrum modulus of the parent signal and the mean spectrum of the generated signals, considering a subdivision of the frequency domain in M=1,5,10 constant-intensity-bandwidths, assuming two correlation structures Λ_ω and Λ_τ: Landers earthquake.

of spectral variations in the signal, which can be appropriate when seeking an overview rather than a detailed representation of spectral changes.

The choice of the number of bands can be made by examining the characteristics of the seismic signal being analysed. If the signal has rapid and significant frequency changes, it may be useful to use multiple bands to capture these variations accurately. Conversely, if the frequency variations of the signal are less pronounced, fewer bands may be sufficient. Another critical factor to take into account when deciding on the number of frequency bands in wavelet analysis is the availability of computational resources. The process of dividing the frequency domain into a greater number of bands demands a commensurate increase in computational power. Conversely, when confronted with constraints in computational resources, it becomes necessary to make a more discerning choice regarding the number of frequency bands. Therefore, it is necessary to find a trade-off between computational efficiency and the level of detail captured in the analysis. In fact, it's crucial to strike a balance that aligns with the available resources while still meeting the analytical goals. Another crucial consideration in the selection of the number of frequency bands for the wavelet analysis is the required level of precision. In applications where precision is of utmost importance, such as structural engineering, the choice of a greater number of frequency bands can significantly enhance the accuracy of the analysis. This heightened level of granularity ensures that even the subtlest spectral details are meticulously captured and accounted for. This precision is indispensable when the analysis directly impacts safety, design, or performance assessments of critical structures. Conversely, in applications where a high degree of precision is not as critical, a more moderate number of bands might sufficient. This approach provides a balanced trade-off between computational efficiency and precision, ensuring that the analysis remains suitable for its intended purpose.

Another fundamental point concerns the choice of the type of correlation structure to adopt. Various intermediate models can be considered for random phases. Unlike the correlation structure used in Section 5 to generate random phases in a simple test signal, Section 6 introduces a distinct correlation structure for generating random phases when the parent signal is a seismic accelerogram. This new structure links the distance between two wavelet centers to fundamental seismic parameters of the parent earthquake ground motion, which are: significant duration and frequency bandwidth. Through the formulation introduced in Section 4, it is possible to evaluate the statistics of the generated random process for any correlation structure adopted.

In this paper, for the first time in the literature, the versatility of circular harmonic wavelets has been exploited to generate samples of fully non-stationary random processes. The use of the circular harmonic wavelets allows higher frequency resolution since its

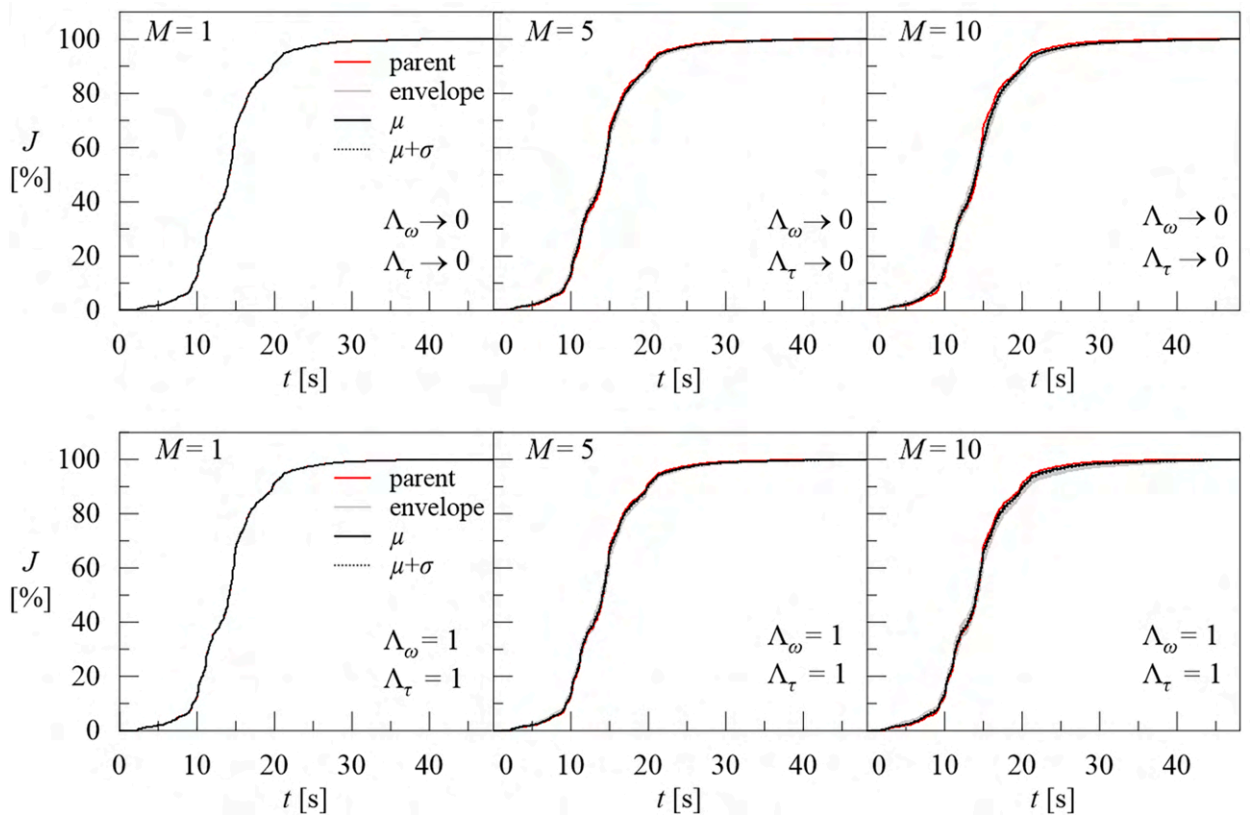

Fig. 17. Percentage Husid's function of the parent accelerogram together with the statistics of the generated signals, considering a subdivision in M=1,5,10 constant-intensity-bandwidths, assuming two different correlation measures Λ_ω and Λ_τ: Landers earthquake.

bandwidth could be artificial controlled. However, a drawback of the proposed method is the absence of a unique solution for determining the width of the frequency bands.

The main advantage of the proposed method is that by varying the frequency domain partition and introducing the correlation structure, it becomes possible to generate samples with the desired time and frequency characteristics. However, a limitation of the proposed method is that it is designed to replicate the characteristics of a 'seed' ground motion used for calibration, rather than to generate simulations for arbitrary future earthquake scenarios.

Based on the numerical results, the following recommendations are made for the application of the proposed method:

- divide the frequency domain in constant-intensity-bandwidths (CIB), evaluated as the frequencies corresponding to the value released by cumulative distribution of the seismic signal in the frequency domain, normalised with respect to the Arias intensity $\widetilde{J}(\omega)$;
- select the number of bands based on the shape of the function $\widetilde{J}(\omega)$ of the parent signal. In fact, the width of the frequency bands should be capable of capturing the changes in slope of the aforementioned function, as illustrated by the vertical lines in Fig. 5;
- the use of the partially-correlated structure, by setting $\Lambda_\omega = \Lambda_\tau = 1$ in the function introduced in Eq. (44) is recommended for the generation of samples when the parent signal is a seismic accelerogram.

7. Conclusions and future research

In this study, the circular harmonic wavelet transform has been used to randomly generate an arbitrary number of seismic records with similar non-stationary characteristics as a "parent" signal, without the need to preliminary define a target evolutionary power spectral density (PSD) function. Specifically, a recorded accelerogram is decomposed into the superposition of complex-valued harmonic wavelets, and an expedient extension of the well-known *Shinozuka's formula* is used to randomize their phases. In the present work, a new correlation structure has been introduced for the random phases, which leads to the generation of "child" samples having different forms of variability with respect to the parent accelerogram, i.e., a random realization of a zero-mean Gaussian process, representative of the expected seismic action. In particular, the use of a vector of zero-mean, Gaussian variables with unitary variance,

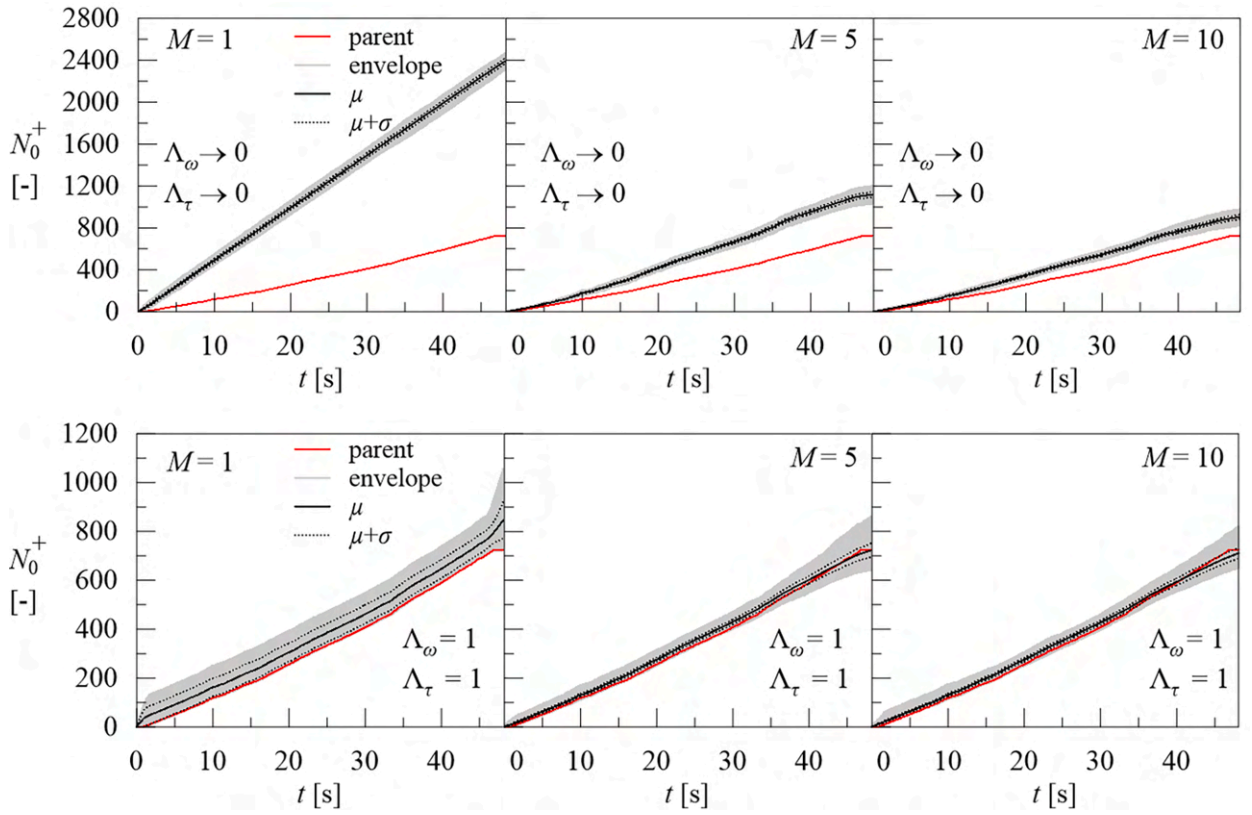

Fig. 18. Cumulative zero level up crossing function of the parent accelerogram together with the statistics of the child signals, considering a subdivision in M=1,5,10 constant-intensity-bandwidths, assuming two correlation measures Λ_ω and Λ_τ: Landers earthquake.

has been used to obtain a vector colleting the partially-correlated random phases trought a suitable variable transformation.

The numerical results have evidenced the critical role played by the choice of number and size of the bands partitioning the frequency domain. For instance, assuming that the random phases are statistically independent and considering the two extreme cases, either with a single frequency band or several mono-frequency bands, leads to random processes in which information on the energy distribution is lost in the frequency or time domain, respectively. Instead, the assumption of a convenient time–frequency correlation structure for the random phases lets the designer preserve all the desired non-stationary characteristics of the parent signal and obtain an effective trade-off between time and frequency localization.

Based on the above considerations, it is worth emphasizing here that the proposed wavelet-based procedure can be seen as a practical engineering tool to achieve an optimal compromise in preserving the parent's information in the time and frequency domains. As a matter of fact, adopting an extreme approach, focused on just one of the two domains, is not able to deliver useful results for seismic design purposes.

Further study will be required to ascertain the effects of the wavelet-based generation on the seismic response of non-linear structures.

CRediT authorship contribution statement

Federica Genovese: Writing – review & editing, Writing – original draft, Visualization, Validation, Software, Methodology, Investigation, Formal analysis, Data curation, Conceptualization. **Alessandro Palmeri:** Writing – review & editing, Writing – original draft, Visualization, Validation, Supervision, Methodology, Investigation, Formal analysis, Data curation, Conceptualization.

Declaration of competing interest

The authors declare that they have no known competing financial interests or personal relationships that could have appeared to influence the work reported in this paper.

Furthermore, the views and conclusions expressed in this paper are solely those of the authors and do not necessarily represent the views or positions of the organizations which they are affiliated with.

Data availability

Data will be made available upon reasonable request.

Appendix A. General procedure for the generation of random phases

The vector of random phases $\boldsymbol{\phi} = \left\{\phi_{1,0}, ..., \phi_{j,k}, ..., \phi_{M,b_M-1}\right\}^{\mathrm{T}}$ required to generate the samples of the discrete random process F_ℓ (see Eqs. (14) and (15)) could in general be a mix of uncorrelated, partially correlated and fully correlated random variables. If the generic random phases $\phi_{j,k}$ and $\phi_{J,K}$ are fully correlated, i.e., $\phi_{j,k} \equiv \phi_{J,K}$, the corresponding ith and Ith rows and columns (see Eq. (27)) in the $N \times N$ covariance matrix $\sum_{\phi\,\phi} = \mathbb{E}\left[\boldsymbol{\phi} \cdot \boldsymbol{\phi}^{\mathrm{T}}\right]$ are equal to each other. Given the transformation of Eq. (25), the same occurs with the ith and Ith rows and columns of the $N \times N$ covariance matrix of the auxiliary random variables $\boldsymbol{u} = \{u_1, ..., u_i, ..., u_N\}^{\mathrm{T}}$, given by (see Eqs. (20) and (30)):

$$\sum_{\boldsymbol{uu}} = \mathbb{E}\left[\boldsymbol{u} \cdot \boldsymbol{u}^{\mathrm{T}}\right] = 2\sin\left(\frac{1}{2\pi}\sum_{\phi\,\phi}\right). \tag{A.1}$$

When two or more random phases are fully correlated, thus, the matrix $\Sigma_{\boldsymbol{uu}}$ is not positive definite, hindering the application of standard techniques for the generation of Gaussian random vectors. To overcome this problem, let's introduce the $N \times \widehat{N}$ Boolean matrix $\boldsymbol{\beta}$, $\widehat{N}$ being the number of random phases without any repetitions in the covariance matrix $\boldsymbol{\Sigma}_{\boldsymbol{\phi\phi}}$; that is, $\widehat{N}$ is the rank of the matrix $\boldsymbol{\Sigma}_{\boldsymbol{\phi\phi}}$. The generic element of the matrix $\boldsymbol{\beta}$ satisfies the conditions:

$$\beta_{i,h} = \begin{cases} 1, & \text{if } u_i \equiv u_h; \\ 0, & \text{otherwise}, \end{cases} \tag{A.2}$$

where $1 \le i \le N$ and $1 \le h \le \widehat{N} = \mathrm{rank}\left(\boldsymbol{\Sigma}_{\boldsymbol{\phi}\,\boldsymbol{\phi}}\right) \le N$.

The vector of the sought random phases can then be expressed as:

$$\boldsymbol{\phi} = \Phi(\boldsymbol{\beta} \cdot \widehat{\boldsymbol{u}}) = \boldsymbol{\beta} \cdot \Phi(\widehat{\boldsymbol{u}}), \tag{A.3}$$

where $\widehat{\boldsymbol{u}} = \{\widehat{u}_1, ..., \widehat{u}_h, ..., \widehat{u}_{\widehat{N}}\}^{\mathrm{T}}$ is the reduced auxiliary vector of zero-mean, Gaussian variables with unitary variance. Its covariance matrix is definite positive and can be obtained by dropping the $N - \widehat{N}$ rows and columns corresponding to the redundant fully correlated random phases. Formally, this can be expressed as:

$$\sum_{\hat{\boldsymbol{u}}\hat{\boldsymbol{u}}} = \mathbb{E}\left[\widehat{\boldsymbol{u}} \cdot \widehat{\boldsymbol{u}}^{\mathrm{T}}\right] = \boldsymbol{\beta}^{+} \cdot \sum_{\boldsymbol{uu}} \cdot \boldsymbol{\beta}^{+\mathrm{T}}, \tag{A.4}$$

In which $\boldsymbol{\beta}^{+}$ is the $\widehat{N} \times N$ pseudo-inverse of the Boolean matrix $\boldsymbol{\beta}$, such that $\boldsymbol{\beta}^{+} \cdot \boldsymbol{\beta} = \boldsymbol{I}_{\widehat{N}}$, $\boldsymbol{I}_{\widehat{N}}$ being the identity matrix of size $\widehat{N}$, and $\boldsymbol{\beta}^{+\mathrm{T}} = \left[\boldsymbol{\beta}^{+}\right]^{\mathrm{T}}$. Being definite positive, the covariance matrix of Eq. (A.4) can be used to generate samples of the reduced auxiliary random vector $\widehat{\boldsymbol{u}}$, which are then transformed into the samples of the random phases $\boldsymbol{\phi}$ through Eq. (A.3).

References

[1] D.M. Boore, J.J. Bommer, Processing of strong-motion accelerograms: Needs, options and consequences, Soil Dyn. Earthq. Eng. 25 (2005) 93–115, https://doi.org/10.1016/j.soildyn.2004.10.007.

[2] Y. Bozorgnia, N.A. Abrahamson, L.A. Atik, T.D. Ancheta, G.M. Atkinson, J.W. Baker, A. Baltay, D.M. Boore, K.W. Campbell, B.S.J. Chiou, R. Darragh, S. Day, J. Donahue, R.W. Graves, N. Gregor, T. Hanks, I.M. Idriss, R. Kamai, T. Kishida, A. Kottke, S.A. Mahin, S. Rezaeian, B. Rowshandel, E. Seyhan, S. Shahi, T. Shantz, W. Silva, P. Spudich, J.P. Stewart, J. Watson-Lamprey, K. Wooddell, R. Youngs, NGA-West2 Research Project, Earthq Spectra 30 (2014) 973–987, https://doi.org/10.1193/072113EQS209M.

[3] C.A. Goulet, T. Kishida, T.D. Ancheta, C.H. Cramer, R.B. Darragh, W.J. Silva, Y.M. Hashash, J. Harmon, G.A. Parker, J.P. Stewart, R.R. Youngs, PEER NGA-East Database. Earthquake Spectra 37 (2021) 1331–1353, https://doi.org/10.1177/87552930211015695.

[4] L. Luzi, R. Puglia, E. Russo, M. D'Amico, C. Felicetta, F. Pacor, G. Lanzano, U. Çeken, J. Clinton, G. Costa, L. Duni, E. Farzanegan, P. Gueguen, C. Ionescu, I. Kalogeras, H. Özener, D. Pesaresi, R. Sleeman, A. Strollo, M. Zare, The engineering strong-motion database: A platform to access pan-European accelerometric data, Seismol. Res. Lett. 87 (2016) 987–997, https://doi.org/10.1785/0220150278.

[5] A. Arias, A measure of earthquake intensity, in: R.J. Hansen (Ed.), Seismic Design for Nuclear Power Plants, MIT Press, Cambridge, UK, 1970, pp. 438–483.

[6] R. Klein, D. Ingman, S. Braun, Non-stationary signals: Phase-energy approach - Theory and simulations, Mech Syst Signal Process 15 (2001) 1061–1089, https://doi.org/10.1006/mssp.2001.1398.

[7] G. Muscolino, F. Genovese, G. Biondi, E. Cascone, Generation of fully non-stationary random processes consistent with target seismic accelerograms, Soil Dyn. Earthq. Eng. 141 (2021) 106467, https://doi.org/10.1016/j.soildyn.2020.106467.

[8] G. Chen, M. Beer, Y. Liu, Modeling response spectrum compatible pulse-like ground motion, Mech Syst Signal Process 177 (2022) 109177, https://doi.org/10.1016/j.ymssp.2022.109177.

[9] H. Hong, X. Cui, D. Qiao, Simulating nonstationary non-Gaussian vector process based on continuous wavelet transform, Mech Syst Signal Process 165 (2022) 108340, https://doi.org/10.1016/j.ymssp.2021.108340.

[10] D. Wang, F. Yu, F. Kong, J. Xu, Simulation of fully nonstationary random processes using generalized harmonic wavelets, Mech Syst Signal Process 181 (2022) 109468, https://doi.org/10.1016/j.ymssp.2022.109468.
[11] F. Genovese, B. Biondi, E. Cascone, G. Muscolino, Energy-compatible modulating functions for the stochastic generation of fully non-stationary artificial accelerograms and their effects on seismic site response analysis, Earthq Eng Struct Dyn 52 (2023) 2682–2707, https://doi.org/10.1002/eqe.3889.
[12] B. Peng, J. Xu, Y. Peng, Efficient simulation of multivariate non-stationary ground motions based on a virtual continuous process and EOLE, Mech Syst Signal Process 184 (2023) 109722, https://doi.org/10.1016/j.ymssp.2022.109722.
[13] G. Muscolino, F. Genovese, A. Sofi, Reliability bounds for structural systems subjected to a set of recorded accelerograms leading to imprecise seismic power spectrum, ASCE-ASME J RISK U A 8 (2022) 04022009, https://doi.org/10.1061/AJRUA6.0001215.
[14] K. Trevlopoulos, C. Feau, I. Zentner, Parametric models averaging for optimized non-parametric fragility curve estimation based on intensity measure data clustering, Struct. Saf. 81 (2019) 101865, https://doi.org/10.1016/j.strusafe.2019.05.002.
[15] X.Y. Cao, D.C. Feng, Y. Li, Assessment of various seismic fragility analysis approaches for structures excited by non-stationary stochastic ground motions, Mech Syst Signal Process 186 (2023) 109838, https://doi.org/10.1016/j.ymssp.2022.109838.
[16] F. Genovese, G. Muscolino, A. Palmeri, Effects of stochastic generation on the elastic and inelastic spectra of fully non-stationary accelerograms, Probabilistic Eng. Mech. 71 (2023) 103377, https://doi.org/10.1016/j.probengmech.2022.103377.
[17] D.E. Newland, An Introduction to Random Vibrations, Spectral & Wavelet Analysis, 3rd edition ed.,, Prentice Hall, Harlow, Essex, England: New York, 1993.
[18] J. Chen, F. Kong, Y. Peng, A stochastic harmonic function representation for non-stationary stochastic processes, Mech Syst Signal Process 96 (2017) 31–44, https://doi.org/10.1016/j.ymssp.2017.03.048.
[19] F. Genovese, T. Alderucci, G. Muscolino, Design sensitivity analysis of structural systems with damping devices subjected to fully non-stationary stochastic seismic excitations, Comput Struct 284 (2023) 107067, https://doi.org/10.1016/j.compstruc.2023.107067.
[20] K. Gurley, A. Kareem, Applications of wavelet transforms in earthquake, wind and ocean engineering, Eng. Struct. 21 (1999) 149–167, https://doi.org/10.1016/S0141-0296(97)00139-9.
[21] P.D. Spanos, G. Failla, N. Politis, Wavelets - Concepts and applications, in: Vibration and Shock Handbook. CRC Press, Boca Raton, FL, USA, 11:1–11–24, 2005.
[22] D. Cecini, A. Palmeri, Spectrum-compatible accelerograms with harmonic wavelets, Comput Struct 147 (2015) 26–35, https://doi.org/10.1016/j.compstruc.2014.10.013.
[23] D.E. Newland, Harmonic wavelet analysis, Proceedings of the Royal Society of London. Series A: Mathematical and Physical Sciences 443 (1993), 203–225. https://doi.org/10.1098/rspa.1993.0140.
[24] D.E. Newland, Harmonic and musical wavelets. Proceedings of the Royal Society of London. Series A: Mathematical and Physical Sciences 444 (1994), 605–620. https://doi.org/10.1098/rspa.1994.0042.
[25] P.D. Spanos, G. Failla, Evolutionary spectra estimation using wavelets, J Eng Mech 130 (2004) 952–960, https://doi.org/10.1061/(ASCE)0733-9399(2004)130:8(952).
[26] P.D. Spanos, J. Tezcan, P. Tratskas, Stochastic processes evolutionary spectrum estimation via harmonic wavelets, Comput Methods Appl Mech Eng 194 (2005) 1367–1383, https://doi.org/10.1016/j.cma.2004.06.039.
[27] P. Spanos, I. Kougioumtzoglou, Harmonic wavelets based statistical linearization for response evolutionary power spectrum determination, Probabilistic Eng. Mech. 27 (2012) 57–68, https://doi.org/10.1016/j.probengmech.2011.05.008.
[28] M.B. Priestley, Spectral Analysis and Time Series, Academic Press, London, 1981. Volumes I and II.
[29] J. Liang, S.R. Chaudhuri, M. Shinozuka, Simulation of nonstationary stochastic processes by spectral representation, J Eng Mech 133 (2007) 616–627, https://doi.org/10.1061/(ASCE)0733-9399.
[30] A. Der Kiureghian, J. Crempien, An evolutionary model for earthquake ground motion, Struct. Saf 6 (1989) 235–246, https://doi.org/10.1016/0167-4730(89)90024-6.
[31] F.G. Fan, G. Ahmadi, Nonstationary Kanai-Tajimi models for El Centro 1940 and Mexico City 1985 earthquakes, Probabilistic Eng. Mech. 5 (1990) 171–181, https://doi.org/10.1016/0266-8920(90)90018-F.
[32] C.H. Yeh, Y. Wen, Modeling of nonstationary ground motion and analysis of inelastic structural response, Struct. Saf. 8 (1990) 281–298, https://doi.org/10.1016/0167-4730(90)90046-R.
[33] J. Beck, C. Papadimitriou, Moving resonance in nonlinear response to fully nonstationary stochastic ground motion, Probabilistic Eng. Mech. 8 (1993) 157–167, https://doi.org/10.1016/0266-8920(93)90011-J.
[34] B. Basu, V.K. Gupta, Seismic response of SDOF systems by wavelet modeling of nonstationary processes, J Eng Mech 124 (1998) 1142–1150, https://doi.org/10.1061/(ASCE)0733-9399(1998)124:10(1142).
[35] B. Basu, V.K. Gupta, Non-stationary seismic response of MDOF systems by wavelet transform, Earthq Eng Struct Dyn 26 (1997) 1243–1258, https://doi.org/10.1002/(SICI)1096-9845(199712)26:12<1243::AID-EQE708>3.0.CO;2-P.
[36] Y.Y. Tang, Wavelet theory approach to pattern recognition, 74, in Series in machine perception and artificial intelligence 2nd ed., World Scientific, New Jersey, OCLC: ocn327142051, 2009.
[37] J. Iyama, H. Kuwamura, Application of wavelets to analysis and simulation of earthquake motions, Earthq Eng Struct Dyn 28 (1999) 255–272, https://doi.org/10.1002/(SICI)1096-9845(199903)28:3<255::AID-EQE815>3.0.CO;2-C.
[38] A. Giaralis, P. Spanos, Wavelet-based response spectrum compatible synthesis of accelerograms - Eurocode application (EC8), Soil Dyn. Earthq. Eng. 29 (2009) 219–235, https://doi.org/10.1016/j.soildyn.2007.12.002.
[39] P.D. Spanos, A. Giaralis, J. Li, Synthesis of accelerograms compatible with the Chinese GB 50011–2001 design spectrum via harmonic wavelets: artificial and historic records, Earthq. Eng. Eng. Vib. 8 (2009) 189–206, https://doi.org/10.1007/s11803-009-9017-4.
[40] J. Legrue, C. Menun, Simulation of nonstationary ground motions using wavelets, in: 13th World Conference on Earthquake Engineering, Vancouver, BC, Canada, 1 (2004), Paper 296.
[41] P. Cacciola, I. Zentner, Generation of response-spectrum-compatible artificial earthquake accelerograms with random joint time–frequency distributions, Probabilistic Eng. Mech. 28 (2012) 52–58, https://doi.org/10.1016/j.probengmech.2011.08.004.
[42] A. Preumont, The generation of non-separable artificial earthquake accelerograms for the design of nuclear power plants, Nucl. Eng. Des. 88 (1985) 59–67, https://doi.org/10.1016/0029-5493(85)90045-7.
[43] P. Cacciola, P. Colajanni, G. Muscolino, Combination of modal responses consistent with seismic input representation, J Struct Eng 130 (2004) 47–55, https://doi.org/10.1061/(ASCE)0733-9445(2004)130:1(47)x.
[44] M. Nakamura, F. Sasaki, K. Yokoyama, T. Tamaoki, A. Tanabe, W. Mizumachi, M. Yamada, Generation of artificial earthquake motion using observed earthquake motions, in: 14th World Conf. on Earthquake Eng., 2008, pp. 1–8.
[45] F. Sasaki, T. Maeda, Y. Yamamoto, Artificial ground motion with non-stationarity generated using the wavelet analysis. Proc of the 17th Structural Mechanics in Reactor Technology, 2003.
[46] G. Amiri, A. Shahjouei, S. Saadat, M. Ajallooeian, M., Hybrid evolutionary-neural network approach in generation of artificial accelerograms using principal component analysis and wavelet-packet transform, J. Earthq. Eng. 15 (1) (2011) 50–76.
[47] Y. Yamamoto, J.W. Baker, Stochastic model for earthquake ground motion using wavelet packets, Bull. Seismol. Soc. Am. 103 (6) (2013) 3044–3056, https://doi.org/10.1785/0120120312.
[48] C. Vlachos, K.G. Papakonstantinou, G. Deodatis, Predictive model for site specific simulation of ground motions based on earthquake scenarios, Earthq Eng Struct Dyn 47 (1) (2018) 195–218, https://doi.org/10.1002/eqe.2948.
[49] C. Vlachos, K.G. Papakonstantinou, G. Deodatis, Structural applications of a predictive stochastic ground motion model: Assessment and use, 04018006, ASCE-ASME J RISK U A 4 (2) (2018), https://doi.org/10.1061/AJRUA6.0000946.
[50] S. Rezaeian, A. Der Kiureghian, Simulation of synthetic ground motions for specified earthquake and site characteristics, Earthq Eng Struct Dyn 39 (10) (2010) 1155–1180, https://doi.org/10.1002/eqe.997.

[51] M. Shinozuka, C.M. Jan, Digital simulation of random processes and its applications, J Sound Vib. 25 (1) (1972) 111–128.
[52] M. Shinozuka, G. Deodatis, Simulation of stochastic processes by spectral representation, Appl Mech Rev 44 (1991) 191–204, https://doi.org/10.1115/1.3119501.
[53] G. Deodatis, Non-stationary stochastic vector processes: seismic ground motion applications, Probab Eng Mech. 11 (3) (1996) 149–167.
[54] J. Liang, S.R. Chaudhuri, M. Shinozuka, Simulation of nonstationary stochastic processes by spectral representation, J Eng Mech 133 (6) (2007) 616–627.
[55] K. Kanai, Semi-empirical formula for the seismic characteristics of the ground, Bull Earthquake Res Inst, Tokyo University 35 (1957) 309–325.
[56] H.A. Tajimi, A statistical method of determining the maximum response of building structure during an earthquake, In: Proc. of the 2nd WCEE, Tokyo and Kyoto, 2 (1960), 1960:781-798.
[57] C. Vlachos, K.G. Papakonstantinou, G. Deodatis, A multi-modal analytical non-stationary spectral model for characterization and stochastic simulation of earthquake ground motions, Soil Dyn. Earthq. Eng. 30 (2016) 177–191, https://doi.org/10.1016/j.soildyn.2015.10.006.
[58] P. Cacciola, G. Deodatis, A method for generating fully non-stationary and spectrum-compatible ground motion vector processes, Soil Dyn. Earthq. Eng. 31 (3) (2011) 351–360, https://doi.org/10.1016/j.soildyn.2010.09.003.
[59] P. Wen, R. Liu, R. Wen, Wavelet packets-based simulation of non-stationary multivariate ground motions, Probabilistic Eng. Mech. 74 (2023) 103495, https://doi.org/10.1016/j.probengmech.2023.103495.
[60] Y. Ohsaki, On the significance of phase content in earthquake ground motions, Earthq. Eng. Struct. Dyn. 7 (5) (1979) 427–439, https://doi.org/10.1002/eqe.4290070504.
[61] Z. Hou, Y. Zhou, M.F. Dimentberg, M. Noori, A non-stationary stochastic model for periodic excitation with random phase modulation, Probabilistic Eng. Mech. 10 (2) (1995) 73–81, https://doi.org/10.1016/0266-8920(95)00002-G.
[62] M. Shrikhande, V.K. Gupta, On the characterisation of the phase spectrum for strong motion synthesis, J. Earthq. Eng. 5 (04) (2001) 465–482, https://doi.org/10.1080/13632460109350402.
[63] M. Shinozuka, G. Deodatis, Stochastic process models for earthquake ground motion, Probabilistic Eng. Mech. 3 (1988) 114–123, https://doi.org/10.1016/0266-8920(88)90023-9.
[64] K. Gkoktsi, A. Giaralis, Effect of frequency domain attributes of wavelet analysis filter banks for structural damage localisation using the relative wavelet entropy index, Int. J. Sustain. Mater. Struct. Syst. 2 (1–2) (2015) 134–160, https://doi.org/10.1504/IJSMSS.2015.078365.
[65] S. Mallat, A Wavelet Tour of Signal Processing: The Sparse Way, 3rd edition, Elsevier, Amsterdam, 2009.
[66] L. Cohen, Time-Frequency Analysis, First Edition, Pearson College Div, 1994.
[67] S. Qian, Introduction to Time-Frequency and Wavelet Transforms, First Edition, Prentice Hall, 2001.
[68] D.C. Montgomery, G.C. Runger, Applied Statistics and Probability for Engineers. EMEA edition, 7th edition ed., Wiley, Hoboken, NJ, 2018.
[69] P.D. Spanos, J. Tezcan, P. Tratskas, Stochastic processes evolutionary spectrum estimation via harmonic wavelets, Comput. Methods Appl. Mech. Eng. 194 (12–16) (2005) 1367–1383, https://doi.org/10.1016/j.cma.2004.06.039.
[70] M. Falk, A simple approach to the generation of uniformly distributed random variables with prescribed correlations, Commun. Stat. Simul. Comput. 28 (1999) 785–791, https://doi.org/10.1080/03610919908813578.
[71] R. Husid, H. Medina, J. Rios, Análisis de terremotos norteamericanos y japoneses. Revista del Centro de Investigación, Desarrollo e Innovación de Estructuras y Materiales (IDIEM) 8 (1969), 28. (in Spanish).
[72] J.J. Bommer, A. Martínez-Pereira, The effective duration of earthquake strong motion, J. Earthq. Eng. 3 (1999) 127–172, https://doi.org/10.1142/S1363246999000077.
[73] M.D. Trifunac, A.G. Brady, A study on the duration of strong earthquake ground motion, Bull. Seismol. Soc. Am. 65 (1975) 581–626, https://doi.org/10.1785/BSSA0650030581.
[74] B. Kedem, On frequency detection by zero-crossings, Signal Process. 10 (1986) 303–306, https://doi.org/10.1016/0165-1684(86)90107-6.
[75] S. Kay, R. Sudhaker, A zero crossing-based spectrum analyzer, IEEE Trans. Signal Process, IEEE Transactions on Acoustics, Speech, and Signal Processing 34 (1986) 96–104, https://doi.org/10.1109/TASSP.1986.1164784.
[76] T. Sreenivas, R. Niederjohn, Zero-crossing based spectral analysis and SVD spectral analysis for formant frequency estimation in noise, IEEE Transactions on Signal Processing 40 (1992) 282–293, https://doi.org/10.1109/78.124939.
[77] M.D. Trifunac, Zero baseline correction of strong-motion accelerograms, Bull. Seismol. Soc. Am. 61 (5) (1971) 1201–1211, https://doi.org/10.1785/BSSA0610051201.
[78] M.D. Trifunac, F.E. Udwadia, A.G. Brady, Analysis of errors in digitized strong-motion accelerograms, Bull. Seismol. Soc. Am. 63 (1) (1973) 157–187, https://doi.org/10.1785/BSSA0630010157.
[79] D.M. Boore, Effect of baseline corrections on displacements and response spectra for several recordings of the 1999 Chi-Chi, Taiwan, earthquake, Bull. Seismol. Soc. Am. 91 (5) (2001) 1199–1211, https://doi.org/10.1785/0120000703.
[80] D.M. Boore, J.J. Bommer, Processing of strong-motion accelerograms: needs, options and consequences, Soil Dyn. Earthq. Eng. 25 (2) (2005) 93–115, https://doi.org/10.1016/j.soildyn.2004.10.007.
[81] E.M. Rathje, B.A. Abrahamson, J.D. Bray, Simplified frequency content estimates of earthquake ground motions, J Geotech Geoenviron 124 (2) (1998) 150–159, https://doi.org/10.1061/(ASCE)1090-0241(1998)124:2(150).